

1 Strain engineering in metal halide perovskite 2 materials and devices: Influence on stability 3 and optoelectronic properties

5 Cite as: Chem. Phys. Rev. **2**, 000000 (2021); doi: [10.1063/5.0044588](https://doi.org/10.1063/5.0044588)

6 Submitted: 17 January 2021 · Accepted: 18 June 2021 ·

7 Published Online: 0 Month 0000



9 AQ1 Mengru Wang, Zhenyi Ni, Xun Xiao, Ying Zhou, and Jinsong Huang^{a)} 

10 11 AFFILIATIONS

12 Department of Applied Physical Sciences, University of North Carolina, Chapel Hill, North Carolina 27599, USA

13 ^{a)}Author to whom correspondence should be addressed: jhuang@unc.edu

ABSTRACT

14 Metal halide perovskites (MHPs) have been extensively studied for their promising applications in solar cells and other devices due to
15 their extraordinary optoelectronic properties, low cost, and easy fabrication by versatile processes. Different from bulk crystals
16 grown from solutions, polycrystalline perovskite films deposited on substrates generally are strained due to multiple mechanisms,
17 which significantly impact their optoelectronic properties, defect physics, and photostability. The fabrication and operation of

18 perovskite solar panels inevitably introduce strains in perovskite. Strain has been broadly applied to stabilize the photoactive phase of
19 several perovskite compositions that would otherwise show a thermodynamically stable photoinactive phase at room temperature.
20 There is increasing research on strain engineering of MHPs to enhance device performance. However, a systematic review and
21 understanding of strain engineering in MHP is still lacking. Herein, an overview of strain engineering on MHP materials and solar cells
22 is provided. In this review, we start with a general review on strain in semiconductors, including the characteristics of strain,
23 characterization techniques, and the effects of strain on the lattice structure, electronic, and optical properties of semiconductors. We
24 then summarize progress in understanding the generation of strain categorized by local and global strains and their impacts on the
25 multi-faceted properties of MHPs, including phase stability, photostability, and other optoelectronic properties. Both positive and nega-
26 tive impacts have been observed on these properties. Strain engineering has shown to be promising in making much more efficient and
27 stable perovskite solar cells.

Published under an exclusive license by AIP Publishing. <https://doi.org/10.1063/5.0044588>

28 TABLE OF CONTENTS

30 I. INTRODUCTION	1
32 II. STRAIN CHARACTERIZATION.....	3
33 A. X-ray diffraction	4
35 B. TEM	4
38 C. Raman spectroscopy.....	4
39 III. STRAIN ENGINEERING IN METAL HALIDE	
40 PEROVSKITES.....	4
43 A. Strain in perovskites.....	4
45 1. Local strain	4
46 2. Global strain	5
48 B. Impact of strain on properties of perovskites.....	8
50 1. Influence of strain on perovskite structures...	8
52 2. Influence of strain on optoelectronic	
54 properties of perovskites	12

IV. SUMMARY AND OUTLOOK	14	56
Experiment and Methods	14	58

59 I. INTRODUCTION

60 Metal halide perovskites (MHPs) have attracted much attention
61 due to their high defect tolerance, low trap density, high optical
62 absorption coefficients, high carrier mobility, long carrier lifetime, and
63 tunable bandgap.^{1–6} The low-cost, low-temperature scalable solution
64 fabrication processes have also promoted the wide application of
65 MHPs in photovoltaics, light-emitting diodes, photodetectors, lasers,
66 and ion radiation detectors.^{7–12} It is notable that the power conversion
67 efficiency (PCE) of single-junction perovskite solar cells has been rap-
68 idly enhanced from 3.8% to 25.5% in 10 years,^{13,14} which is higher
69 than those of other thin film photovoltaics such as CdTe and CIGS,

70 and is approaching the best efficiency of monocrystalline single crystal
71 silicon solar cells.

72 Strain, as one very important variable that defines the material's
73 deformation, plays an important role in the fundamental properties and
74 application of semiconductors, which should impact MHPs. The effect
75 of strain on semiconductor properties has been widely exploited since
76 the influence of strain on the intrinsic mobility of Si was first investigated
77 in the early 1950s.¹⁵⁻¹⁸ It developed into a field of strain engineering,
78 which refers to the method of improving one or more properties of
79 materials through mechanical deformations. Strain is a tensor to describe
80 and quantify the deformation of a material. Generally, there are compo-
81 nents along the diagonal (normal strain) and off diagonal terms (shear
82 strain) in a strain tensor. Strain in materials can be classified into four
83 types according to the loading applied to the material [Fig. 1(a)]: uniaxial
84 strain (a material is stretched or compressed along one direction), biaxial
85 strain (a material is pulled or compressed in two directions), hydrostatic
86 strain (the deformation of a material in all normal directions under load-
87 ing is equal and no shear components and thereby only changes the vol-
88 ume of the material, but not in shape), and shear strain (the deformation
89 of a material results from forces acting along the material's two parallel
90 surfaces.); meanwhile, due to Poisson's effect, strain was also induced in
91 non-loading direction. A deformed material can have a combination of
92 these different types of strain. Based on the distribution range of the
93 strain, it can also be classified as global and local strains. A global strain
94 means that the strain is introduced across the entire material, which
95 mainly originates from lattice mismatch or thermal expansion coefficient
96 mismatch between materials and the substrates [Figs. 1(b)-1(c)]. In epi-
97 taxy growth of materials, if the lattice constant (α_1) of material 1 is
98 larger/smaller than that of material 2 (α_2), an in-plane biaxial compres-
99 sive/tensile strain is induced in material 1. For materials involving in
100 thermal annealing processes, if the thermal expansion coefficient of
101 material 1 (α_1) is larger/smaller than that of material 2 (α_2), an in-plane
102 biaxial tensile/compressive strain is induced in material 1. The deforma-
103 tion of substrates will also induce strain in pre-deposited materials. For
104 example, bending the substrates could induce in-plane uniaxial tensile/
105 compressive strain related to the bending direction in the materials
106 [Fig. 1(d)]. Elongating the substrate could also induce in-plane uniaxial
107 tensile strain in pre-deposited materials [Fig. 1(e)]. Although the range
108 of global strain is the entire material, the global strain can be either
109 homogeneous or inhomogeneous across the whole material. For exam-
110 ple, thermal gradient induces inhomogeneous global strain in materials.
111 In the epitaxial growth of semiconductors, the largest strain is at the het-
112 eroepitaxial interface, and strain decreases at the regions away from the
113 interface. As the strain energy increases, it would become energetically
114 favorable to form dislocations. Strain relaxation occurs along with the
115 generation of these dislocations. While bending materials to induce uni-
116 axial strain, all materials on one side of the neutral axis are under ten-
117 sion, while those on the other side are under compression, and there is
118 no strain along the neutral axis. The location of neutral axis of the lay-
119 ered structure depends on the sample structure, including the thick-
120 nesses and mechanical properties of functional layers and substrates.¹⁹
121 The bending strain is a function of bending curvature and the distance
122 from the neutral axis: $\epsilon = h/\rho$, where ρ is the bending curvature of the
123 material and h is the distance from the neutral axis. So, there is a strain
124 gradient from top to bottom across the cross-section, and the maximum
125 strains occur on the material surfaces. A local strain means that the
126 strain is not uniform through the material, only locating in certain

127 regions. As shown in Fig. 1(f), depositing materials on elastically pre-
128 deformed substrates first and then releasing the substrates result in a
129 local strain in the wrinkling or buckling regions of the material. Besides,
130 local strain can also be induced by elemental doping or alloying due to
131 the size difference between the dopant and the host atoms [Fig. 1(g)].

132 Strain in semiconductors is embodied in the extension or short-
133 ening of chemical bond lengths, and/or the change of chemical bond
134 angles, which leads to changes in crystal volume and/or the distortion
135 of the lattice of crystals. Such a distortion can cause a phase transition.
136 Theoretical and experimental work has demonstrated that strain
137 could change the crystal structure of Si, Ge, and two-dimensional
138 transition metal chalcogenides, resulting in a phase transition.²⁰⁻²³
139 For example, a small (0.2%) tensile strain has been shown to trans-
140 form hexagonal semiconducting MoTe₂ (~1 eV bandgap) into metal-
141 lic phase (distorted octahedra).²³ The changed lattice constant by
142 strain should change the interatomic interaction as well, resulting in a
143 change in bandgap. For example, in most semiconductors, a compres-
144 sive strain would make the bonding and antibonding energy states
145 further apart in energy, resulting in a wider bandgap. Furthermore,
146 the influence of strain on the conduction band and valence band may
147 be different, and thus induces direct-indirect transitions in semicon-
148 ductors such as two dimensional MoS₂.²⁴⁻²⁶ At the same time, the
149 changed band structure in strained semiconductors inevitably
150 impacts the curvature of the dispersion relation at the band edges.
151 The effective mass (m^*) of carriers is determined by the band curva-
152 ture and thus changes with strain, which also impacts carrier mobili-
153 ties. For example, the carrier mobility in Si NWs is very responsive to
154 strain and can be enhanced or reduced by a factor 2-5 for moderate
155 uniaxial strains within the $\pm 2\%$ range due to the changes in the
156 effective mass (m^*) of carriers.²⁴ Strain can also impact the defect
157 density in materials. Strain could change the vacancies concentration
158 in semiconductors by changing its formation energy. For example,
159 the tensile strained MoS₂ has a decreased bandgap and increased S
160 vacancy concentrations,²⁷ leading to an unprecedentedly catalytic
161 activity of MoS₂ for the hydrogen evolution reaction. Strain has also
162 been proved to control the O vacancy concentrations by changing the
163 formation energy of O vacancies in transition-metal oxide materi-
164 als.^{28,29} For example, the oxygen content of perovskite-based stron-
165 tium cobaltite (SrCoO_{3-x}) shifts from $x < 0.1$ to $x \sim 0.25$ when
166 modest amounts of tensile strain over 1% was induced in materials.²⁸

167 Strain engineering is an effective tool to tune material properties
168 for its pronounced impact on lattices. Notably, strain in semiconduc-
169 tors is inevitable introduced in material fabrication for either lattice
170 mismatch with substrates or lattice expansion/contraction during ther-
171 mal annealing process. Hence, studying the strain effect would provide
172 insight in understanding and designing MHPs for solar cell applica-
173 tions. Compared with traditional semiconductors such as Si and
174 GaAs, MHPs have a relatively low Young's modulus (10-30 GPa) and
175 a large ratio of bulk modulus to shear modulus (bulk modulus/shear
176 modulus > 1.75), which may enable flexible perovskite devices, includ-
177 ing flexible solar cells, light emitting diodes, and detectors.³⁰⁻³³ The
178 soft nature of MHPs makes them more sensitive to stress than other
179 semiconductor materials, since the strain is greater under the same
180 stress in MHPs. Residual tensile strain has been commonly observed
181 in thermally annealed perovskite films.^{34,35} Changing local strain using
182 alloying has been shown to successfully enhance the performance of
183 perovskite solar cells, including efficiency and stability.³⁶ Therefore,

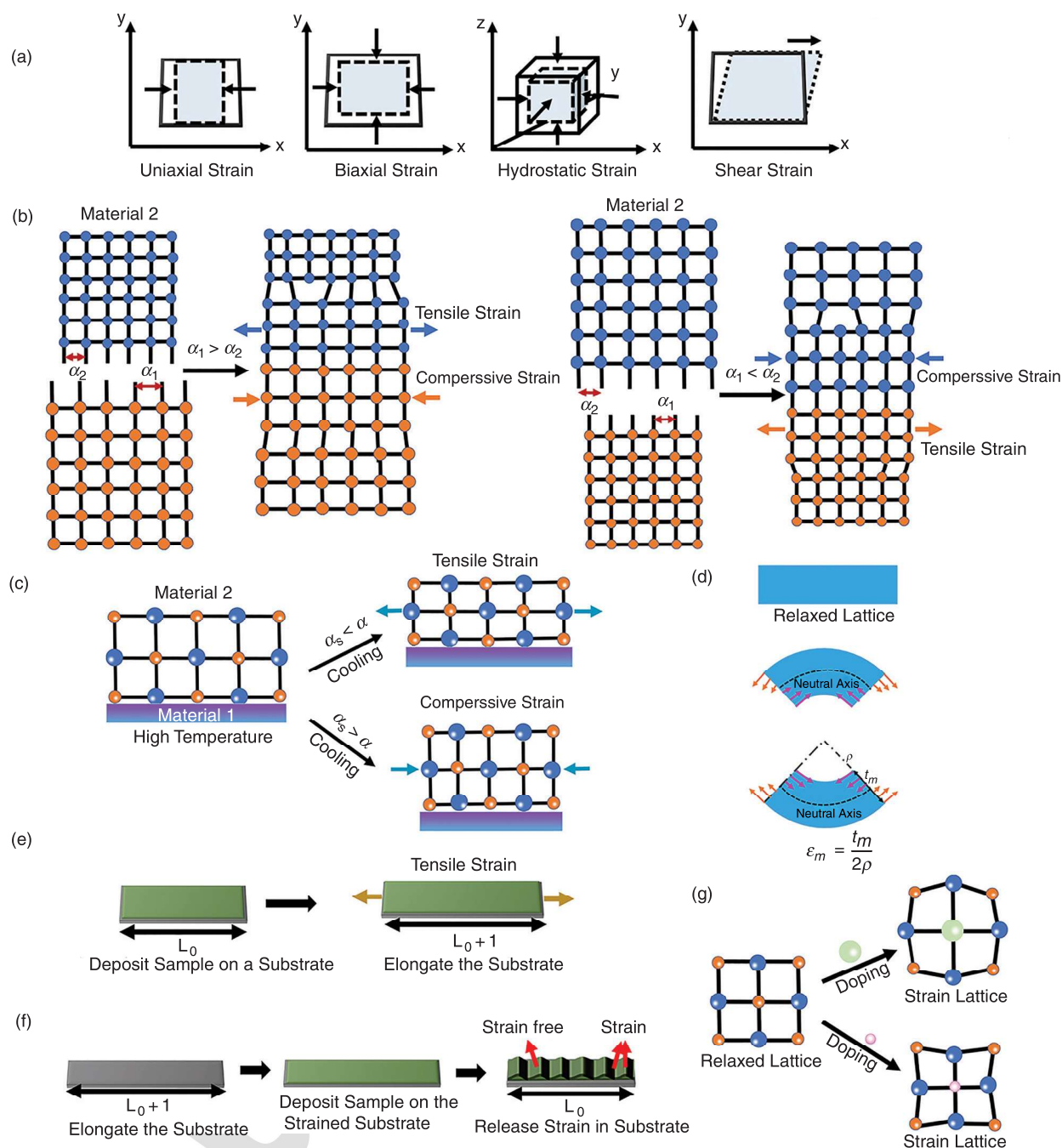


FIG. 1. (a) Schematic of $\langle 100 \rangle$ uniaxial, (x-y) plane biaxial, and hydrostatic strain. Schematic of methods to induce strain: (b) lattice mismatch; (c) thermal expansion coefficients mismatch; (d) bending the substrates; (e) elongating substrate to induce uniaxial tensile strain; (f) releasing strain in the pre-deformed substrate; (g) chemical doping or substitution or absorption.

184 strain engineering in perovskite has aroused great interest in research.
 185 This review summarizes the progress in understanding the effect of
 186 strain on phase stability, bandgap, and trap density in MHPs and
 187 future research prospects.

II. STRAIN CHARACTERIZATION

188 The first step to understand the impact of strain on materials is
 189 to accurately characterize the strain. The strain in semiconductors can
 190

191 be directly characterized through the lattice distortion by x-ray diffraction 244
 192 (XRD) and transmission electron microscopy (TEM) measurements. And it can also be indirectly quantified through the changes of 245
 193 the optical properties of semiconductors that are characterized by 246
 194 Raman spectroscopy. Here, we summarize these three commonly used 247
 195 techniques for strain characterizations. 248
 196

197 A. X-ray diffraction

198 XRD technique is a widely used method to characterize lattice 249
 199 structures with high resolutions, which can directly measure the global 250
 200 strain without the destruction of the sample.³⁷ Strain in materials will 251
 201 induce lattice contraction/expansion or tilting. Correspondingly, XRD 252
 202 peaks shift to a larger/smaller diffraction angle under compressive/tensile 253
 203 strain. In addition, the diffraction peak is broadened when the 254
 204 strain is not homogeneous in materials. Moreover, x-ray microdiffraction 255
 205 method was employed to measure the strain with a sub-micro 256
 206 spatial resolution, which is three orders of magnitude higher than that 257
 207 of conventional XRD techniques, and the strain-resolution ($\Delta\epsilon$) 258
 208 reaches 10^{-5} .^{37,38} Generally, x-ray technique requires a volume of 259
 209 materials (more than tenths of a gram), thus it is unfeasible for the 260
 210 analysis of the lattice information of individual nanosized materials. 261

211 B. TEM

212 TEM technique is a powerful technique to characterize strain, 262
 213 which typically has a spatial resolution up to 0.1–0.2 nm with a precision 263
 214 of 10^{-3} .³⁹ Strain is characterized by measuring the changes in 264
 215 local lattice constants and orientations of the lattice planes with respect 265
 216 to reference materials. Considering the immediate damage of the 266
 217 materials by the energetic electron beam, cryo-TEM has been applied 267
 218 in the structural characterization of materials that are prone to be 268
 219 damaged by electron beam (e.g., perovskites).^{40,41} In addition, low- 269
 220 dose scanning TEM is also used to determine the microstructure of 270
 221 perovskite thin films to slow down the degradation from the same total 271
 222 electron beam.⁴² Notably, it is still challenging to prepare TEM samples, 272
 223 which should be thin enough to become sufficiently transparent 273
 224 to electrons. The samples are usually thinned by ion-beams, which 274
 225 may introduce damage or changes to the strain of samples, leading to 275
 226 an inaccurate characterization of the strain.^{39,43} 276

227 C. Raman spectroscopy

228 Raman spectroscopy is a nondestructive chemical analysis technique 277
 229 to study the stress/strain of materials based on the interaction of 278
 230 the laser with the chemical bonds in a material.⁴⁴ Strain in materials 279
 231 leads to the changes in lattice vibration (phonon), which can be 280
 232 detected by Raman spectroscopy. The vibrational frequency shift is 281
 233 shown to be proportional to strain magnitude in materials.^{45–49} In tensile 282
 234 strained materials, phonon softens and the vibrational frequency 283
 235 decreases in the strain direction, leading to a red-shifting of the 284
 236 Raman peaks. Conversely, compressive strain leads to phonon hardening 285
 237 and a blue-shifting of Raman peaks.⁴⁵ The capability of mapping 286
 238 using Raman allows the mapping of strain with a spatial resolution 287
 239 better than 0.5 μm and a sensitivity better than 10^{-3} .⁴⁴ Also, it does 288
 240 not require sophisticated sample preparation, ensuring undistorted 289
 241 strain states in materials. In Raman spectroscopy, great consideration 290
 242 should be paid to the excitation laser wavelength and intensity, 291
 243 because they affect both the Raman signal depth profile and 292

244 intensity.⁵⁰ In addition, low-power laser is needed to avoid laser- 245
 245 heating effects and sample degradation. For example, laser excitation 246
 246 power with less than 10 μW on spot diameter of 1 μm was reported in 247
 247 Raman measurement of laser-sensitive perovskites, which is 2 orders 248
 248 of magnitude lower than $\mu\text{c-Si:H}$ thin films.^{51,52} 249

249 It should be noted that the Raman peak shifting is not only 250
 250 related to the strain in materials; changes in physical or chemical envi- 251
 251 ronments will also cause the shifts of Raman peaks. The dependence 252
 252 of peak frequency and full width at half-maximum (FWHM) on defect 253
 253 density and grain sizes have also been demonstrated.⁵³ Therefore, it is 254
 254 important to control experimental conditions precisely and combine 255
 255 other strain characterization methods to characterize strain in 256
 256 materials. 257

III. STRAIN ENGINEERING IN METAL HALIDE 257 PEROVSKITES 258

A. Strain in perovskites 259

1. Local strain 260

261 In ABX₃ structured perovskites, the mismatch between the A cat- 261
 262 ions and BX₆ cage size leads to cage distortions and BX₆ octahedra tilt- 263
 263 ing, inducing local strain in perovskites. Goldschmidt's tolerance 264
 264 factor (τ) is widely used in predicting the structural stability and octa- 265
 265 hedral factor (μ) defines the stability of the BX₆ octahedron.⁵⁴ Both 266
 266 factors are necessary but not sufficient to predict perovskite structural 267
 267 formability. Tolerance factor τ can be expressed by the equation 268

$$\tau = \frac{R_A + R_X}{\sqrt{2(R_B + R_X)^2}}$$
 268
 268 where R_A, R_B, and R_X are the ionic radii of A cation 269
 269 (methylammonium-MA⁺, formamidinium-FA⁺, Cesium-Cs⁺, etc.), 270
 270 B cation (lead-Pb²⁺, tin-Sn²⁺, etc.), and X anion (iodide-I⁻, bromide- 271
 271 Br⁻, chloride-Cl⁻, etc.), respectively. Octahedral factor μ is the ratio of 272
 272 the ionic radius of B and X atoms: $\mu = \frac{R_B}{R_X}$. Perovskites with τ between 273
 273 0.8 and 1.0 and μ between 0.44 and 0.90 are reported to be thermody- 274
 274 namically stable at room temperature.^{54,55} However, perovskites with 275
 275 τ out of this range, such as FAPbI₃ ($\tau > 1$) and CsPbI₃ ($\tau < 0.8$), tend 276
 276 to form the photoinactive hexagonal δ -phase at room temperature. 277
 277 During the spontaneous phase transformation from photoactive 278
 278 perovskite phases to δ -phases, strain is also induced in crystals due to 279
 279 spatial heterogeneity. Saidaminov *et al.* claimed the existence of local 280
 280 strain in black-phase FAPbI₃ (α -FAPbI₃), and it would be released by 281
 281 point defect formations.³⁶ Conversely, Zheng *et al.* proposed that α - 282
 282 FAPbI₃ has an anisotropic strained lattice, and the strain in the (111) 283
 283 plane is greater, which drives phase transformation into the strain-free 284
 284 δ -phase.⁵⁶ The unfavorable residual strain in FAPbI₃ lattice could be 285
 285 released by the substitution or doping of foreign ions (such as MA⁺, 286
 286 Cs⁺, Ca²⁺, Cl⁻ or Br⁻) to form alloyed perovskites.^{36,56–59} However, 287
 287 composition inhomogeneity in alloyed perovskites also leads to local 288
 288 strains. For example, I-Br mixed halide perovskites tend to form I- 289
 289 rich regions and Br-rich regions under illumination when the content 290
 290 of Br is larger than 20%,⁶⁰ which would induce local strain in perov- 291
 291 skites. In polycrystalline perovskite films, grain boundaries are known 292
 292 as reservoirs of defects and likely to change the strain state in their 293
 293 vicinity because of different atomic spacing and structure compared to 294
 294 their perfect crystal structure.⁶¹ In addition, light-induced strain is also 295
 295 reported in FA_{0.7}MA_{0.25}Cs_{0.05}PbI₃ and MAPbI₃ films,^{62,63} originating 296
 296 from photothermal-induced expansion in the perovskite films. Solid 297
 297 material formation kinetics also impact the residual strain in films or 298
 298 crystals. For example, strain can be induced in solution-processed 299

AQ3

299 films due to solvent removal, phase transformation from intermediate
 300 phases, film shrinkage, and volatile component (MA^+ , Cl^-) removal
 301 during annealing.⁶⁴ Therefore, strain distribution is likely to be inho-
 302 mogeneous at atomic scale in perovskite materials. Jones *et al.* probed
 303 local strain in $MAPbI_3$ perovskite thin films by scanning micro-XRD
 304 (μ XRD) and high-resolution TEM. The spatial resolution of the
 305 μ XRD was $\sim 2.5 \mu m$. Subtle shifts in the $\langle 220 \rangle$ and $\langle 222 \rangle$ diffraction
 306 peaks position and broadening illustrated the occurrence of local
 307 structural heterogeneity on the scale of beam resolution. The strain
 308 map for the $\langle 220 \rangle$ diffraction peak showed that the magnitude of
 309 strain is 0.1%–0.2%. They also collected the high-resolution TEM
 310 images from a $70 \times 70 \text{ nm}^2$ region. The electron dose rate of TEM
 311 was ~ 1 –4 electrons $\text{Å}^{-2} \text{ s}^{-1}$. There were different diffraction patterns
 312 from various $10 \times 10 \text{ nm}^2$ regions of the TEM images, demonstrating
 313 the presence of structural heterogeneity in nanoscales.⁶⁵ Local strain in
 314 perovskite films is very complicated and thus needs a much more
 315 comprehensive characterization to provide insight into how the local
 316 strain is controlled by film formation kinetics, material composition,
 317 material morphology, etc.

318 2. Global strain

319 *a. Thermal effect.* Thermal expansion coefficient mismatch
 320 between perovskites and substrates introduces global strain in perov-
 321 skite films during their fabrication processes. The thermal expansion
 322 coefficients of perovskites are approximately one order of magnitude
 323 higher than most of their substrates and charge transport materials
 324 (e.g., ITO glass, Si, SnO_2 , TiO_2 , PTAA, etc.).^{34,35,66–70} In 2017, Zhao
 325 *et al.* first discovered that MHP films fabricated by all methods that
 326 involve thermal annealing, including one-step spin-coating, two-step
 327 spin-coating, and doctor blade-coating, were strained, and the flat
 328 polycrystalline $MAPbI_3$ films have an in-plane tensile strain of 0.47%
 329 after cooling down from 100°C .³⁴ The clamp effect of the substrate
 330 also induces a compressive strain along the out-of-plane direction due
 331 to the Poisson effect. Rolston *et al.* also reported a residual in-plane
 332 tensile stresses in perovskite films in excess of 50 MPa, which is high
 333 enough to deform copper.³⁵ Steele *et al.* used synchrotron-based, graz-
 334 ing incidence, wide-angle x-ray scattering to monitor the crystal dis-
 335 tortion process in $CsPbI_3$ thin film after rapidly cooling it from 330°C
 336 to 100°C and observed a $\sim 1\%$ in-plane tensile strain.⁷¹ The magni-
 337 tude of strain from thermal expansion coefficient mismatch directly
 338 correlates with the annealing temperature of perovskite films.
 339 Reducing the film stress and strain can be accomplished by decreasing
 340 annealing temperatures or selecting substrates with large thermal
 341 expansion coefficients.^{35,72} In addition, the residual tensile strain
 342 can be compensated by introducing a compressive strain. The poly-
 343 [5,5-bis(2-butyloctyl) - (2,2bithiophene)-4,4'-dicarboxylate-alt-5,5'-
 344 2,2'-bithiophene] (PDCBT), possessing a higher thermal expansion
 345 coefficient than perovskites, has been used as the hole transport layer
 346 in n-i-p solar cell structure. The tensile strain in PSCs was com-
 347 pensated by elevating the processing temperature of the hole-transport
 348 layer, leading to a non-strained or even compressively strained
 349 $CsPbI_2Br$ perovskite film.⁷²

350 *b. The epitaxial growth of perovskite.* In perovskite solar cells, lat-
 351 tice mismatch-induced strain is not inevitable, because the growth of
 352 perovskite on charge transport layers or charge transport layers on

perovskite is not epitaxial in most of cases.^{73–76} However, there are
 353 cases where epitaxial growth can occur. The horizontal growth of
 354 strained $CsPbBr_3$ microwires on sapphire substrates has already been
 355 reported, where the $CsPbBr_3$ (110) plane grows on the sapphire (0001)
 356 plane and the in-plane lattice parameter of $CsPbBr_3$ is enlarged by
 357 $\sim 2\%$ at the interface with sapphire.⁷⁴ Chen *et al.* reported the strained
 358 epitaxial growth of halide perovskite single-crystal thin films on
 359 lattice-mismatched halide perovskite substrates.⁷³ They investigated
 360 the strain in α -FAPbI₃ that was epitaxially grown on $MAPbCl_{x}Br_{3-x}$
 361 single crystal substrates with different compositions. An in-plane
 362 biaxial compressive strain as high as 2.4% was detected in the epitaxial
 363 α -FAPbI₃. Chen *et al.* studied confocal photoluminescence spectra at
 364 different locations in an α -FAPbI₃ film of around $3 \mu m$ thick grown
 365 on a $MAPbCl_{1.5}Br_{1.5}$ single crystal substrate and found that the 2.4%
 366 compressive strain decreased to near zero from the interface of
 367 α -FAPbI₃/ $MAPbCl_{1.5}Br_{1.5}$ to the top surface of α -FAPbI₃. It was
 368 because that strain in the epitaxial α -FAPbI₃ is determined not only by
 369 the lattice mismatch between the epilayer and substrate, but also the
 370 strain relaxation mechanisms. The thickness-dependent in-plane XRD
 371 showed that the critical thickness of the 2.4% compressive strained
 372 α -FAPbI₃ film is much smaller than $3 \mu m$, which is close to 100 nm.
 373

374 In addition, the epitaxial growth of α - $CsPbBr_{x}I_{3-x}$ perovskite
 375 after adding PbS colloidal quantum dots (CQDs) in $CsPbBr_{x}I_{3-x}$ films
 376 has been reported.⁷⁷ The crystal structure and the orientation of per-
 377 ovskites relative to PbS CQDs were investigated by high-resolution
 378 TEM. They observed the formation of a perovskite shell at high PbS
 379 CQD concentration, and there was no spacing difference between the
 380 core CQD and the $CsPbBr_2I$ perovskite shell at (1 $\bar{1}$ 1) and (200)
 381 planes, indicating the epitaxially orientational alignment of (1 $\bar{1}$ 1) and
 382 (200) planes for both PbS CQDs and for the $CsPbBr_2I$ [Fig. 2(a)].
 383 Lattice mismatch increases as decreasing the ration of Br in $CsPbBr_{x}I_{1-x}$
 384 generating a larger strain at interfaces.⁷⁷ It was also reported that the
 385 epitaxial growth of α -FAPbI₃ phase was observed during its phase
 386 transformation from the hexagonal δ -FAPbI₃ when it forms epitaxial
 387 heterostructure with FPEA₄PbI₄ layered perovskite.⁷⁶ After adding
 388 FPEA₄PbI₄ layered perovskites in FAPbI₃ perovskite films, TEM
 389 images [Fig. 2(b)] showed that the (002) plane of the layered perovskite
 390 was aligned with the (010) plane of the δ -FAPbI₃ phase, and the larger
 391 interplanar spacing of the δ -FAPbI₃ indicates the presence of tensile
 392 strain at the interface with the layered perovskite. Meanwhile, a semi-
 393 coherent interface between the layered perovskite and the α -FAPbI₃
 394 was observed, where the (111) plane of the grown α -FAPbI₃ orienta-
 395 tionally aligns with the (002) plane of the layered perovskite, implying
 396 that the heteroepitaxial growth of the α -FAPbI₃ crystals occurs during
 397 the phase conversion process, and the compressive strain was applied
 398 to the interfacial α -FAPbI₃ phase.⁷⁶

399 *c. Interface (not epitaxy)/surface stress.* Zhao *et al.* fabricated
 400 large-grained $CsPbBr_3$ perovskite films by two-step sequential deposi-
 401 tion fabrication method and observed the compressive stress along the
 402 in-plane direction. The compressive stress is high enough to induce
 403 strain in $CsPbBr_3$ perovskite films. The compressive stress originated
 404 from lattice mismatch between $PbBr_2$ to $CsPbBr_3$ due to the fact that
 405 the lattice volume is enlarged by 2.18 times during the phase conver-
 406 sion from $PbBr_2$ to $CsPbBr_3$ perovskite.⁷⁸ In addition, lattice mismatch
 407 between perovskite lattices and large cations introduced on the surface
 408 of perovskites, like PEA⁺, GA⁺, also induces strain to perovskite films.⁴⁰⁸

AQ4

AQ5

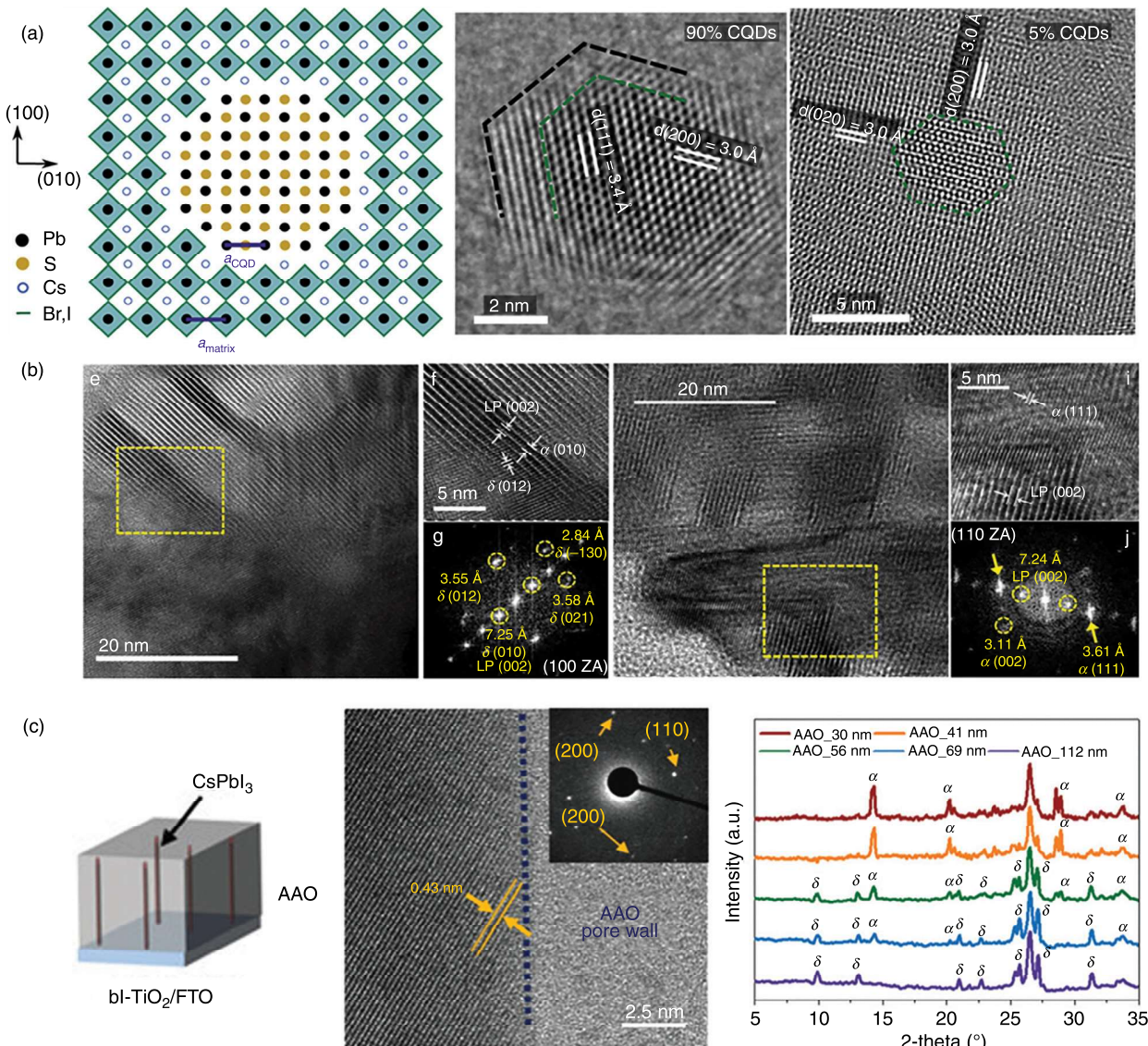


FIG. 2. (a) Schematic depiction of the atomistic model of a PbS CQD:perovskite lattice-anchored hybrid materials system and high-resolution TEM images of the lattice-anchored PbS CQD:perovskite hybrid materials at high (up) and low (down) CQD concentration.¹⁷ Reproduced with permission from Liu *et al.*, *Nature* **570**, 96–101 (2019). Copyright 2019 Nature Publishing Group. (b) High-resolution TEM images and corresponding fast Fourier transform analysis of FAPbI₃ films incorporated with FPEA₄PbI₄ before (left) and after the phase conversion process (right).⁷⁶ Reproduced with permission from Lee *et al.*, *Nat. Commun.* **11**, 5880 (2020). Copyright 2020 Nature Publishing Group. (c) High-resolution TEM image of CsPbI₃ perovskite confined in an AAO template with a pore size of 41 nm (left) and XRD patterns CsPbI₃ perovskite thin films confined in AAO templates (right).⁸⁰ Reproduced with permission from Ma *et al.*, *Small* **15**, 1900219 (2019). Copyright 2019 Wiley-VCH.

409 The soft cation framework of large organic cations buffers the lattice
 410 deformation under residual stress in perovskite films.⁷⁹

411 Ma *et al.* noted that strain was imposed on α -CsPbI₃ perovskites
 412 when they were confined in vertically aligned nanopores of anodized
 413 aluminum oxide (AAO).⁸⁰ As shown in Fig. 2(c), high-resolution
 414 TEM showed that perovskite crystals were confined within 41 nm-size
 415 pores of AAO template, and the (110) plane was sloped at an angle of
 416 35.5° with respect to the AAO pore wall. XRD results exhibited a

reduce in the peak intensity (200)/(110) ratio, indicating enhanced 417 growth of the (110) plane while suppressing the growth of the (200) 418 plane. They thought that the compressive stress imposed by the pore 419 walls was imposed on the [010] and [001] directions of the perovskite 420 lattice, suppressing the growth of the (200) plane-parallel to the pore 421 wall. The compressive stress made the dominant growth orientation of 422 α -CsPbI₃ change to the stress-free [100] direction. The strain magni- 423 tude is dependent on the nanopore size of the AAO template. External 424

425 mechanical stress-induced strain, by hydrostatic pressure and bending
 426 substrates, has also been reported.^{81–85}

427 In perovskite nanoparticles, strain mainly comes from its high
 428 surface tension due to the large surface-to-volume ratio. The tension
 429 and strain magnitude depend on the size of perovskite nanoparticles.⁸⁶
 430 One the other hand, Zhao *et al.* used synchrotron radiation x-ray diffraction
 431 to analyze different shaped CsPbBr₃ nanocrystals with the
 432 same fabrication processes and observed the increasing trend in strain
 433 values of the nanocrystals: nanocube, nanoplate, nanowire. They
 434 thought that the strain reflected the mechanical response of CsPbBr₃
 435 nanoparticles to the stimulus from surrounding liquid organic ligands,
 436 and the result was in good agreement with the nature that nanowires
 437 are easier than nanocubes for bending.⁸⁷ Size-dependent and/or
 438 shape-dependent strain in perovskite nanoparticles and its effect on
 439 nanoparticle properties and devices are interesting topics and need to
 440 be further understood in the future.

441 *d. Ferroelasitity and the photostrictive effect.* Some MHPs have
 442 been determined to be ferroelastic, which can change strain in perov-
 443 skites with an intrinsic path. When an external stress is applied, the
 444 ferroelastic perovskite would dissipate the strain energy by forming
 445 twin structures.^{88,89} This effect makes the strain imposed by external
 446 stress difficult to determine and should be paid attention to during

AQ6 447 research. In addition, the photostrictive effect of halide perovskites has
 448 also been reported, and the photostrictive response was proportional
 449 to the light intensity.^{90,91} However, the photostrictive effect of perov-
 450 skites has been raised to be an experimental artifact which can be
 451 caused by the thermal expansion from the photothermal effect was
 452 underestimated. To distinguish the contribution of strain from photo-
 453 striction and thermal expansion under light in halide perovskites,

Chen *et al.* turned the light (100 mW.cm⁻² white LED) on and off
 454 when the device temperature was kept constant.⁶³ It has been found
 455 that switching the light between on and off conditions for 10 min has
 456 no influence on the position of XRD peaks of MAPbI₃ when tempera-
 457 ture was kept constant. In addition, comparing the thermal expansion
 458 and photostriction on a millisecond timescale, it was still found the
 459 thermal expansion dominated the light-induced strain in MAPbI₃,
 460 with no photostriction detected within equipment sensitivity
 461 limitation.⁹²

462 *e. Device encapsulation and operation.* Photovoltaic (PV) mod-
 463 ules need to be encapsulated. In the encapsulation process, a high tem-
 464 perature of > 100 °C is generally required to cure the encapsulant, and
 465 then assembled layers are pressed together in a laminator to remove
 466 air. During this process, global strain may be introduced into perov-
 467 skite and other layers due to the difference in thermal expansion coef-
 468 ficients of different layers. In addition, pressure from the laminator
 469 can also cause the deformation of the materials.

470 In operation, the working temperature of solar cells varies with
 471 environmental conditions. The environmental temperature can vary
 472 from -40 °C in Arctic areas to 85 °C in desert areas. In addition, the
 473 average temperature in desert areas can be up to 40 °C during the day-
 474 time and fall to -4 °C during nighttime.^{93–96} The capability of solar
 475 cells to keep their integrity is generally examined in the temperature
 476 cycling test part of stability evaluation; however, their impact to the
 477 strain in perovskites and other function layers have not been studied
 478 yet. Besides, hail, snow, and wind in the environment and other exter-
 479 nal mechanical loads can also deform large solar panels. PV modules
 480 are mounted onto a support framework, resulting in the constraints of
 481 displacement and rotation of them. As shown in Fig. 3(b), a PV
 482

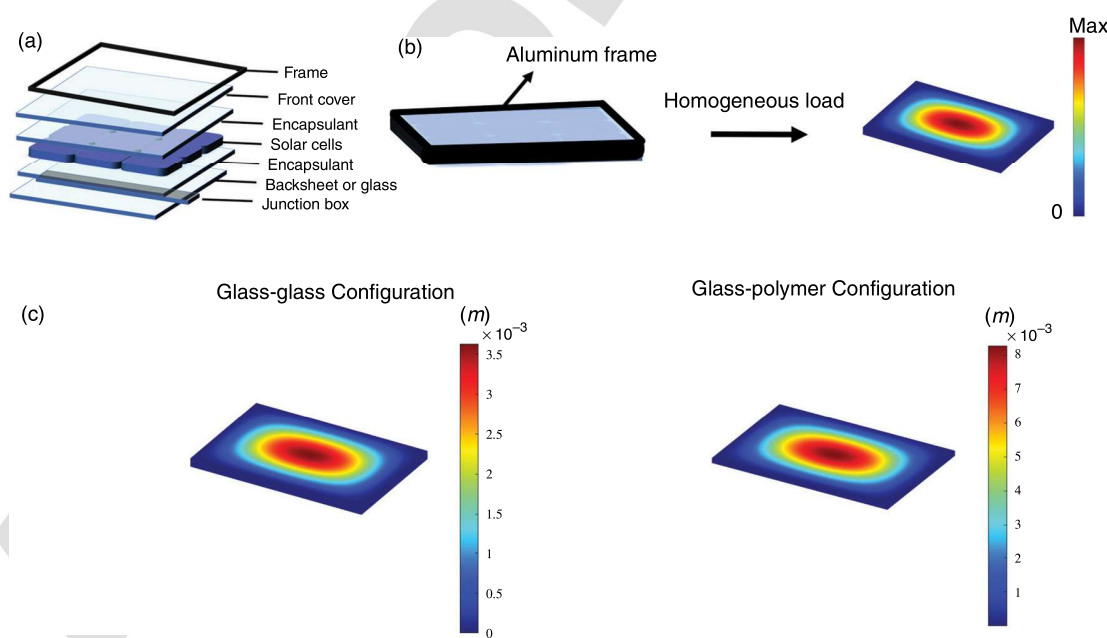


FIG. 3. (a) Structure of PV modules. (b) Displacement distribution on solar panels framed by perimeter under a homogenously distributed load on the front cover. (c) Displacement distribution on glass-glass and glass-polymer solar panels framed by perimeter under 1000 Pa on the front cover.

483 module is fixed on a metal framework by framing perimeters where a
484 homogeneous distributed load is applied on the front cover of PV
485 modules to simulate snow or wind. Using finite element simulation by
486 MATLAB, we show that maximum strain occurs in center of the PV
487 modules, and there is no strain at the constrained region.

Different supporting systems (rigid and flexible) should also have varied effect on strain in PV modules. For flexible frames, strain also occurs in the attached areas in PV modules due to higher flexibility and lower constraint on deformation.⁹⁷ As shown in Fig. 3(c), strain in glass-polymer PV modules is larger than that of glass-glass PV modules when applying the same homogeneously distributed load (1000 Pa). What is more, strain in PV modules could come from the weight of the module itself. When only the weight of the module is considered, strain in glass-glass PV modules is larger than that of glass-polymer PV modules. More simulation can be found elsewhere on thermal and mechanical stress-strain in Si PV modules.^{98,99} The research on strain in perovskite solar cells still at its early stage, which focused on strain engineering in perovskite films. More research at a later stage is needed to find out the strain generation and distribution in perovskite PV modules and their impact.

Table I lists the strain, its magnitude, and influence in metal halide perovskites from recently published experimental work.

505 B. Impact of strain on properties of perovskites

506 1. Influence of strain on perovskite structures

507 *a. Phase transition.* Strain engineering of perovskites could
508 induce the deformation of the crystal structure or phase transitions by
509 distorting the inorganic framework. In the strained epitaxial growth of
510 α -FAPbI₃ films on lattice-mismatched single crystal perovskite sub-
511 strates, reciprocal space mapping of strain-free and strained α -FAPbI₃
512 thin films showed that the increase in the tetragonality of the lattice is
513 evident as the compressive strain increases.⁷³ Under hydrostatic pres-
514 sures, most of perovskite single crystals, like MAPbI₃, MASnI₃,
515 FAPbI₃, CsPbI₃, CsPbCl₃, (PEA)₂PbBr₄, have been reported to
516 undergo phase transition processes, then become amorphous under
517 higher pressures (e.g., 4.1 GPa for FAPbBr₃ single crystal).^{102,103} The
518 magnitude of the pressure needed to induce phase transition and
519 amorphization is different for halide perovskites with different compo-
520 sitions and lattice symmetries, which have different bulk moduli and
521 elastic moduli.

522 *b. Thermodynamics and kinetics of perovskite*
523 **stability. Thermodynamics of phase stability.** Modulating strain is a
524 promising strategy to stabilize photoactive perovskite phases. In perov-
525 skites with tolerance factors out of the range 0.8 to 1, local strain can
526 be changed by incorporating foreign ions, successfully establishing an
527 energetically stable photoactive alloyed perovskite.³⁶ In addition, it has
528 also been observed that the freshly fabricated, black photoactive pure
529 phase perovskite films can be stable on substrates at room temperature
530 for a few minutes. However, once they were scraped from the sub-
531 strate, they would turn into yellow phase immediately.^{34,71} Compared
532 to the strain-free perovskite powders, perovskite films on the substrate
533 have a biaxial tensile strain due to the thermal expansion coefficient
534 differences between the perovskite and the substrate. In CsPbI_3 perov-
535 skite, the introduction of $\sim 1\%$ in-plane biaxial strain leads to different
536 free energy changes for the orthorhombic γ -phase ($\Delta E = 4 \text{ meV}$) and

hexagonal δ -phase ($\Delta E = 31$ meV), making the energy difference promoting the γ -to- δ transition decrease from 85 meV to 58 meV, thus improving the phase stability of γ -phase CsPbI_3 [Fig. 4(a)].⁷¹ Meanwhile, the compressive strained epitaxial α -FAPbI₃ thin film exhibits long-lasting phase stability at room temperature.⁷³ As shown in Fig. 4(b), the sub-100 nm epitaxial α -FAPbI₃ thin film with in-plane 2.4% compressive strain is stable for at least 360 days at room temperature. In contrast, the strain-free α -phase FAPbI₃ immediately turns into the yellow δ phase in only one day. Chen *et al.* proposed two possible mechanisms for the stability of epitaxial α -FAPbI₃ films: the interfacial energy of the α -FAPbI₃/MAPbCl_{3-x}Br_{3-x} single crystal substrate is lower than that of the δ -FAPbI₃/MAPbCl_{3-x}Br_{3-x} single crystal substrate; the compressive strain in the epitaxial α -FAPbI₃ neutralizes the effect of an internal tensile strain, which would induce the formation of vacancies and subsequent phase transition.

Phase transition energy barrier. The influence of strain on the energy barriers for the phase transition between the α -FAPbI₃ and δ -FAPbI₃ was calculated based on the density functional theory (DFT). The calculations confirmed the existence of a potential barrier for the phase transition between α -FAPbI₃ and δ -FAPbI₃.¹⁰⁴ Lee *et al.* found that strain increases the phase transformation energy barrier height of α -phase to δ -phase, and when the FAPbI₃ interlayer spacing decreases from 15.48 Å toward the 15.26 Å, the energy barrier height increased by \sim 0.15 eV from the DFT calculations [Fig. 4(c)].⁷⁶ The increase in energy barrier between α - δ phase will be beneficial for the thermodynamic stability of the α -phase at room temperature. In conclusion, strain engineering can stabilize photoactive perovskite phase.

Ion migration. In strained halide perovskites, local tensile strain reduces the stability of the photoactive perovskite through strain relaxation by the formation of point defects.³⁶ These point defects may be the energetic active sites to react with water and oxygen molecules, thereby accelerating the degradation of perovskites. In addition, tensile strain will reduce the stability of perovskite by accelerating the ion migration, even though it can stabilize α -FAPbI₃ perovskite phase by suppressing the phase conversion to δ -phase. Zhao *et al.* directly measured the ion migration activation energy by temperature conductivity of perovskites under different strain status and verified that the tensile strain in MHPs reduces the activation energy of ion migration.³⁴ Figure 5(a) shows schematic diagram of the different strained MAPbI₃ films by bending substrates. The in-plane biaxial tensile strain in the flat film is about 0.47%. The films were bent in a convex shape to increase the strain to 0.62% or in a concave shape to reduce the strain to 0.2%. When exposing the encapsulated strained film to \sim 50 mW/cm² illumination at 65 °C, the films with 0.63% tensile strain had large areas turned yellow with the appearance of strong PbI₂ peaks, whereas the films with the almost zero tensile strain remained mostly black without any appearance of the PbI₂ peak after 500 h illumination. The accelerated degradation by strain is related to the change of ion migration under strain. In the dark, the activation energies for ion migration are 0.29, 0.39, and 0.53 eV, respectively, and 0.046, 0.074, and 0.083 eV, respectively, under 25 mW/cm² white illumination when tensile stain are 0.62%, 0.47% and 0.2%, respectively. The result conclusively shows that the perovskite films with larger tensile strain have smaller ion migration activation energy in both dark and under illumination conditions. The ion migration accelerates the decomposition of perovskites.

TABLE I. Strain and its magnitude in metal halide perovskites from published experimental work.

Perovskite	Strain origin	Strain magnitude and state (tensile strain +, compressive strain -)	Strain type	Strain effect	Ref.
MAPbI ₃ film	Thermal expansion/bending	0.2%–0.62%	In-plane tensile strain	Global	Thermal expansion induced in-plane tensile strain in perovskite films; 34
MAPbI ₃ film	Thermal expansion	–0.30%	Out-of-plane compressive strain	Global	Tensile strain decreased the activation energy of halide migration and accelerated the degradation of perovskites. Strain patterns have a complex heterogeneity across multiple length scales; strain has a complex local heterogeneity with a magnitude of 0.1–0.2%; 65
CsPbBr ₃ film	Thermal expansion	–1.02%	Out-of-plane compressive	Global	Lattice out-of-plane compressive strain is directly associated with enhanced defect concentrations and non-radiative recombination. 66
CaPbI ₃ film	Thermal expansion	1%	In-plane tensile strain	Global	Out-of-plane strain measured via nano-XRD varies between –0.8 and –1.6%; 71
CsPbI ₂ Br film	Thermal expansion	–1.5%–1%	In-plane strain	Global	Nanoscale residual strains negatively affect the stability of perovskites. 72
Cs _{0.05} MA _{0.16} FA _{0.79} Pb(I _{0.83} Br _{0.17}) ₃ film	Thermal expansion		In-plane tensile	Global	Black phase transformed to the yellow phase through strain release. 73
FAPbI ₃ film	Lattice mismatch	–2.4%–0	In-plane strain	Global	The activation energy of halide ion migration increased, and phase separation was suppressed under compressive strain; PCE enhanced from 14.8% (tensile strain), 15.5% (strain free) to 16% (compressive strain); 74
CsPbBr ₃ nanowire	Lattice mismatch		Out-of-plane compressive	Global	Compressive-strain and non-strain devices retained 96 and 80% of their initial PCEs after 1000 h of heating at 85 °C. Thermal expansion induced in-plane tensile strain and accelerated the degradation of perovskite films; 75
FAPbI ₃ film/ FPEA ₄ PbI ₄	Lattice mismatch			Local	High film stress increased mechanical fragility of perovskite. Compressive strain stabilized black FAPbI ₃ phase over 360 days at room temperature. Strain modulated bandgap of FAPbI ₃ ; Compressive strain enhanced the carrier mobility prominently. 76

TABLE I. (Continued)

PeroVskite	Strain origin	Strain magnitude and state (tensile strain +, compressive strain -)	Strain type	Strain effect	Ref.
PeroVskite				layered perovskite; after phase transition process, compressive strain was induced in the interfacial α phase.	
CaPbI ₃ film	AAO pore wall -stress	-2.5%-0	In-plane strain	Strain increased the phase transition energy barrier, retarding the phase conversion kinetics.	80
CaPbBr ₃ film	Lattice mismatch		Compressive stress	Compressive strain decreased surface formation energy of the α -phase;	78
FAPbI ₃ film	Ion size mismatch		Global	Compressive strain stabilized α -phase over three months under ambient conditions;	
(FAPbI ₃) _{0.85} (MAPbBr ₃) _{0.15} film	A site incorporation		Local	Precise stress control of CsPbBr ₃ film by controlling the crystallization temperature of PbBr ₂ film;	36
PbS CQD: CsPb (Br) ₃ film	Lattice mismatch		Local	Reduced defect-induced charge recombination and enhanced charge transfer under suitable stress.	58
(CH ₃ (CH ₂) ₃ NH ₃) ₂ (CH ₃ -NH ₃) _{n-1} PbI _{3n+1} film	Bending	0-1.18%	Uniaxial tensile strain	Strain relaxation in FAPbI ₃ by forming point defect; Introducing smaller ions, MA/Cs or Br/Cl stabilized perovskite phase and enhanced film stability.	77
(PEA) ₂ PbI ₄ single crystal	Hydrostatic pressure		Global	A site alloying at the surface lattice of perovskite film leads to relaxation of interfacial residual stress;	85
MAPbBr ₃ single crystal	Thermal expansion	-0.3%-0.3%	In-plane strain	Stress relaxation reduced traps on the surface and enhance stability of perovskite films.	100
				The lattice match between QDs and α -phase suppressed the transition to the undesired δ -phase; Perovskite films remained stable for more than six months at ambient conditions;	101
				Carrier mobility was twofold due to a reduced energy barrier for carrier hopping.	
				Tensile strain increases the optical bandgap at a rate of 13.3 meV%.	101
				Ultrabroad tunability of \sim 320 meV by a moderate pressure ranging from 0 to 3.5 GPa.	
				Crystal lattice can strain, relax, or compress as the annealing temperature varies;	
				HOMO levels changed under different strain;	
				The carrier mobility, photocurrent, charge carrier lifetime enhanced under 60 ± 55 °C.	

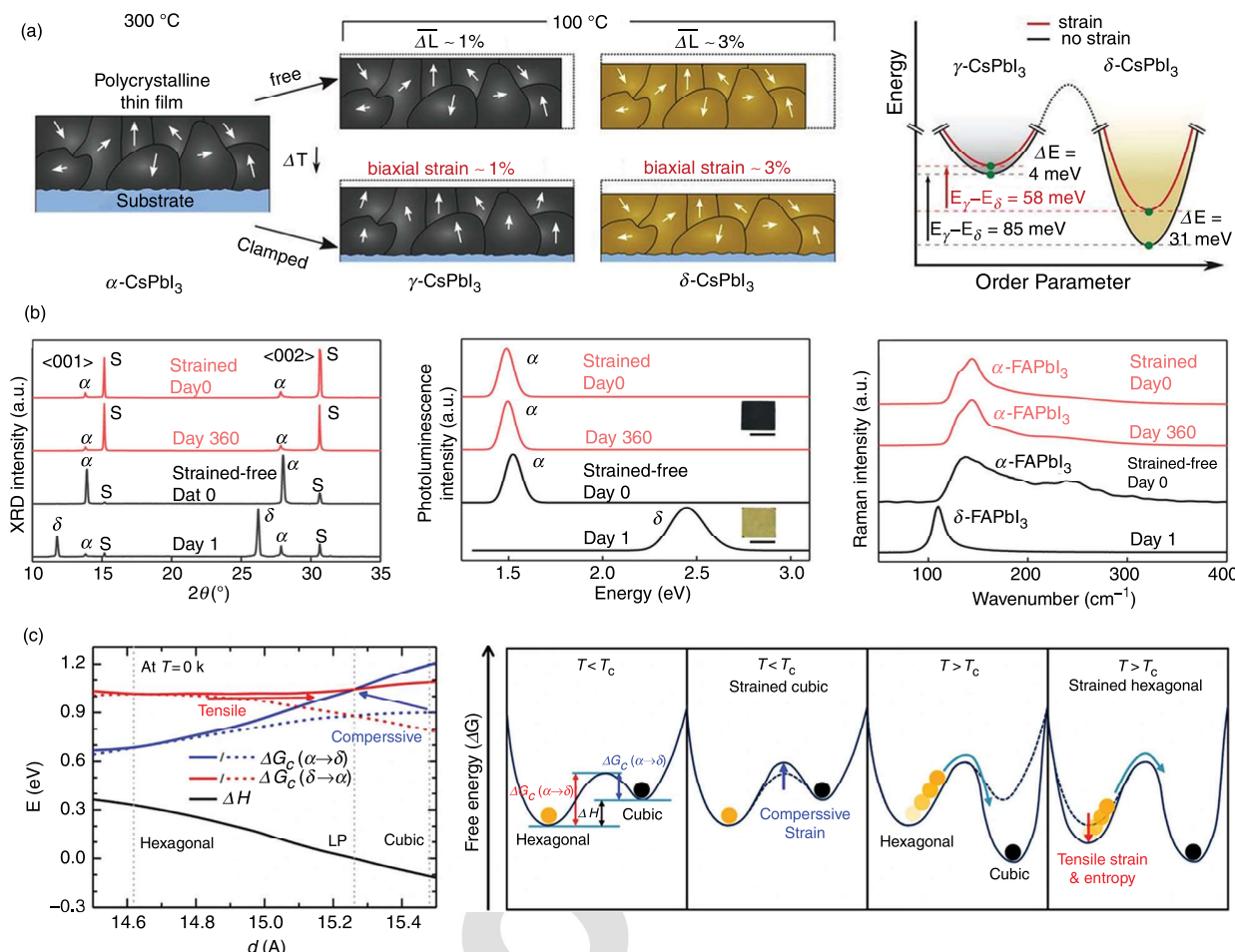


FIG. 4. (a) *Ab initio* energy diagram of the black and yellow CsPbI₃ phases with and without in-plane biaxial strain.⁷¹ Reproduced with permission from Steele *et al.*, *Science* **365** (6454), 679–684 (2019). Copyright 2019 American Association for the Advancement of Science. (b) Phase stability comparison of strained FAPbI₃ film and unstrained FAPbI₃ film.⁷³ Reproduced with permission from Chen *et al.*, *Nature* **577**, 209–215 (2020). Copyright 2020 Nature Publishing Group. (c) DFT-calculated free energy barriers (ΔG_c) for phase conversion (left) and schematic free energy diagrams for the δ - and α -phased FAPbI₃ at compressive strain condition (right) and schematic free energy diagrams for the hexagonal and cubic phased FAPbI₃ at different temperatures and strain condition.⁷⁶ Reproduced with permission from Lee *et al.*, *Nat. Commun.* **11**, 5880 (2020). Copyright 2020 Nature Publishing Group.

594 The ion migration will lead to the phase segregation in mix- 608
 595 halide perovskites, which is detrimental to perovskite material stability. 609
 596 Liu *et al.* obtained near strain-free colloidal PbS quantum dots 610
 597 (CQDs)-CsPbBr₂I perovskite interface. They observed that phase 611
 598 segregation occurred in pristine CsPbBr₂I perovskite films within 30 min 612
 599 after annealing in air at 200 °C. However, this was largely suppressed 613
 600 when PbS CQDs are integrated in CsPbBr₂I at a concentration above 614
 601 6%, and no film degradation was observed after 5 h.⁷⁷ The intensity 615
 602 loss in absorbance and the shift in the absorption edge of unencapsu- 616
 603 lated CQDs-CsPbBr₂I_{1-x} after 5 h of annealing in air (x is the Br 617
 604 content) are shown in Fig. 5(b). For PbS CQD: CsPbBr₂I (x ~ 66%) 618
 605 samples in which near zero lattice mismatch is achieved at the 619
 606 interface of PbS CQDs-CsPbBr₂I, film stability shows a gradual improve- 620
 607 ment with increasing CQD concentrations. Ehrler *et al.* found that 621

when the hydrostatic pressure applied to the perovskite film was 608
 increased to 0.3 GPa,⁸¹ the formation rate of iodide-rich and bromide- 609 rich phases in MAPb(Br_xI_{1-x})₃ decreased by two orders of magnitude.⁶¹⁰
 The results are consistent with calculational work about the tendency 611
 of activation energy for ion migration with strain. The migration bar- 612
 rier of ions increases under compressive strain and decreases under 613
 tensile strain.¹⁰⁵ Compressive strain shortens the length of the Pb–I 614
 bond and enhances the interaction between Pb and I atoms, making it 615
 difficult for I ions to escape from the lattice. As the activation energy 616
 for ion migration increases, phase segregation was suppressed and the 617
 I-vacancy concentration in the perovskite decreases.¹⁰⁶ Notably, mate- 618
 rial stability can decrease significantly when the elastic strain energy in 619
 materials is big enough to induce the formation of misfit or 620
 dislocation.^{107,108} 621

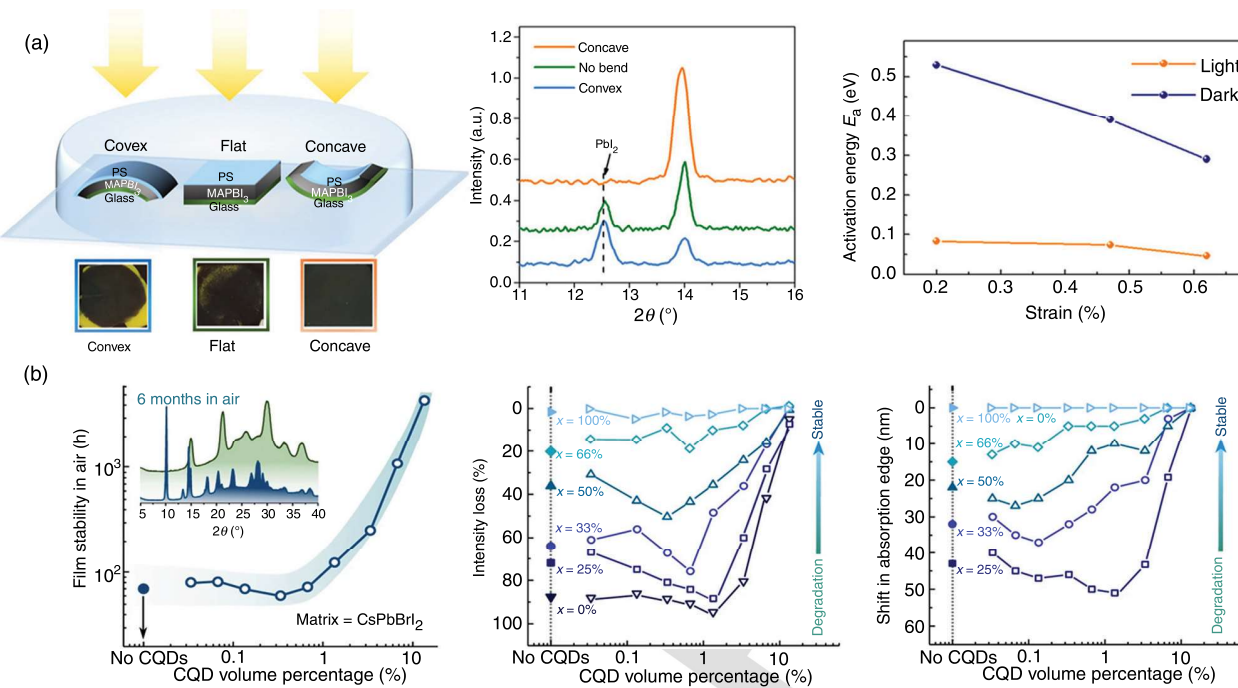


FIG. 5. (a) Schematic illustration of the experimental setup applying different strains and resulting photographs of the corresponding MAPbI₃ films after 500 h of illumination (left); out-of-plane XRD patterns of the MAPbI₃ films with different strains by bending (center) and activation energy of ion migration as a function of the strain level in the MAPbI₃ films.³⁴ Reproduced with permission from Zhao *et al.*, *Sci. Adv.* **3** (5616), eaao5616 (2017). Copyright 2017 American Association for the Advancement of Science. (b) The intensity loss in absorbance (left) and the shift in the absorption edge (right) after 5 h of annealing in air. x is the Br content. Lattice mismatch increases as decreasing Br content and, thus, a larger strain is generated at interfaces; a lower PbS CQD concentration results in more perovskite layers between neighboring PbS CQDs and consequently increases the effects of strain.⁷⁷ Reproduced with permission from Liu *et al.*, *Nature* **570**, 96–101 (2019). Copyright 2019 Nature Publishing Group.

622 2. Influence of strain on optoelectronic properties 623 of perovskites

624 *a. Band structure and carrier mobility.* Alteration in band structure and carrier mobility with strain have been observed in perovskite materials. In most MHPs, the Pb–I orbital coupling contributes 625 directly to the nature of valence and conduction band edges. The A 626 cations do not contribute directly to the formation of band edges, but 627 their size will influence the Pb–I orbital coupling, thus influencing the 628 valence and conduction band edges indirectly. The valence band maximum 629 (VBM) of perovskite is mainly derived from the strong anti- 630 bonding coupling between s orbital of Pb and p orbital of I, and the 631 conduction band minimum (CBM) is mainly derived from the coupling 632 of the Pb p orbital with negligible I.^{3,109} Under a tensile strain, 633 the elongation of Pb–I bonds and/or the reduction of Pb–I–Pb angles 634 will decrease the antibonding overlap between the Pb 6s and I 5p orbitals, 635 causing the downshift of VBM and thus the broadening of the 636 bandgap. Under a compressive strain, the shortened Pb–I bonds will 637 enhance the coupling between the Pb s and I p orbitals and lift the 638 VBM, resulting in a reduction of the bandgap. With the further 639 increase in the compressive strain, the decrease in Pb–I–Pb bond angles 640 and resulting inorganic octahedral tilting start to dominate, which will 641 weaken the Pb 6s and I 5p orbital overlap, thereby downshifting the 642 VBM and increasing the perovskite bandgap.^{106,110,111} Cases where 643 strain alters the bandgap have been reported. When the hydrostatic 644 pressure of 2.1 GPa was applied to the α -FAPbI₃ single crystal, its 645 bandgap reduced from 1.489 eV to 1.337 eV.¹¹² Tu *et al.* applied in- 646 plane uniaxial tensile strain to $(\text{CH}_3(\text{CH}_2)_3\text{NH}_3)_2(\text{CH}_3\text{–NH}_3)_{n-1}$ 647 Pb_nI_{3n+1} 2D perovskite flakes and found that its bandgap increases as 648 the strain increases, and the strain response of bandgap could be as 649 high as 13.3 meV for one percent of strain.⁸⁵ The photoluminescence 650 peak of sub-100-nm epitaxial α -FAPbI₃ thin films gradually shifted 651 from about 1.523 eV at 0% strain to about 1.488 eV at –2.4% strain, 652 corresponding to a reduction of about 35 meV in the bandgap.⁷³ 653 Clearly, the changes in bandgap under strain are different and dependent 654 on the composition of the perovskite.

655 Change of the carrier mobility as a function of strain has also 656 been studied.^{73,113,114} Figure 6(a) shows the calculated effective mass 657 (m*) of electron and hole of a α -FAPbI₃ perovskite and the band struc- 658 tures of the perovskite with the strains of 3%, 0%, and –3%.⁷³ The 659 effective mass of electron (m_e*) remains basically unchanged with the 660 change in strain, while the effective mass of hole (m_h*) decreases con- 661 siderably with the increase in the compressive strain. The reduced m_h* 662 under compressive strain enhances the hole mobility until the com- 663 pressive strain is up to –1.2%, as measured from Hall effect measure- 664 ments and time-of-flight measurements in Figs. 6(b)–6(c).⁷³ The 665 sharp drop in hole mobility above –1.2% strain is attributed to the 666 higher dislocation density at higher strains.

667 In MHPs, the spin–orbit coupling effect contributes strongly to 668 the band splitting in perovskites at different strain due to the existence 669 of the spin-orbit coupling effect. The band splitting in perovskites at 670 different strain due to the existence of the spin-orbit coupling effect.

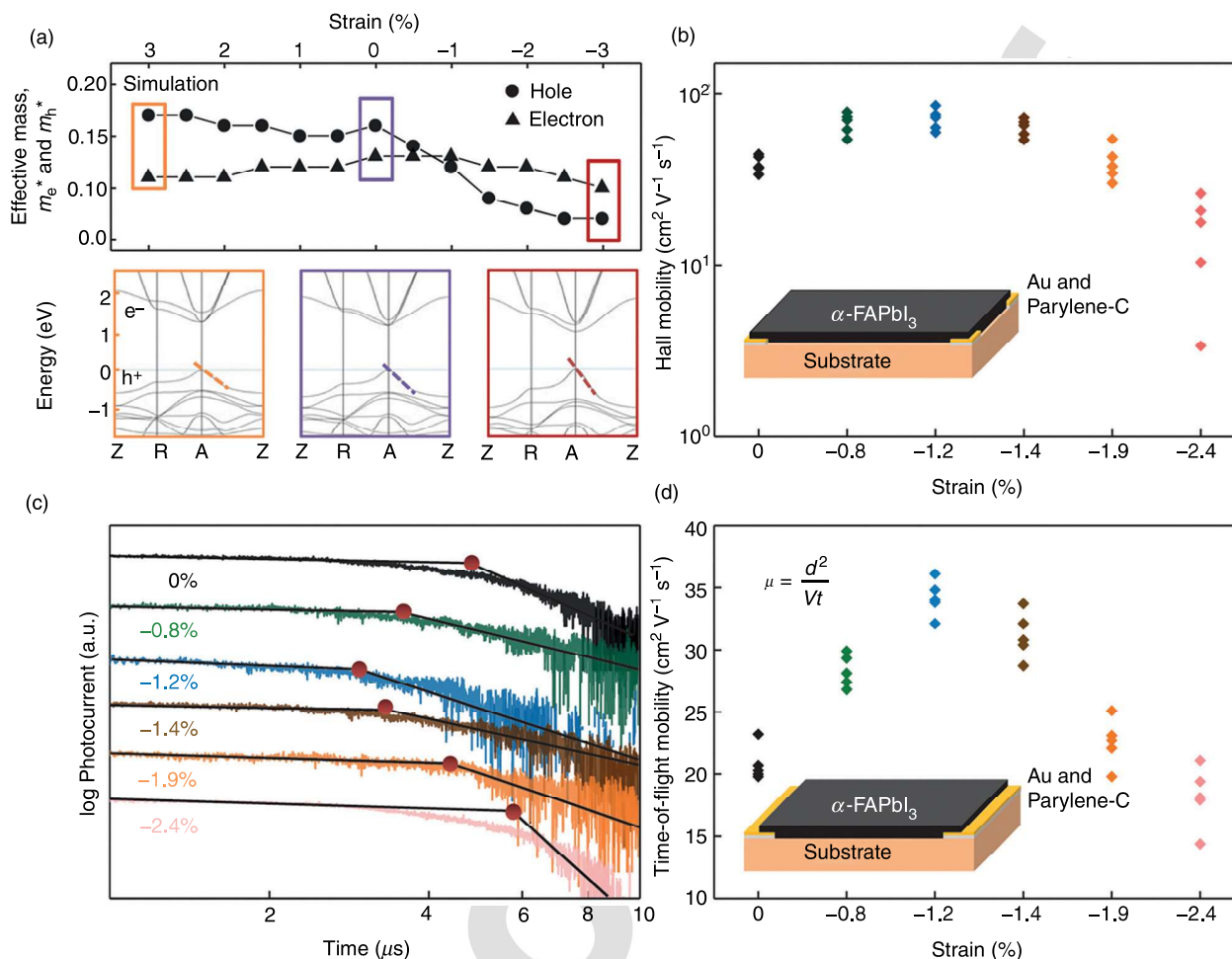


FIG. 6. (a) Calculated effective masses of the carriers at different strains, and electronic band structures under three strain levels (3%, 0%, and -3%). (b) Hole mobilities by Hall effect measurements under different strain. (c) Transient photocurrent curves of the epitaxial α -FAPbI₃ under different strains. (d) Plots of calculated carrier mobilities as a function of the strain magnitudes.⁷³ Reproduced with permission from Chen *et al.*, *Nature* **577**, 209–215 (2020). Copyright 2020 Nature Publishing Group.

of the heavy Pb or Sn atoms.^{115,116} Strain induces transition between direct and indirect bandgap in perovskite due to the different spin-splitting behaviors of CBM and VBM.^{117,118} Ghosh *et al.* used *ab initio* simulations to investigate the Rashba-splitting effect and the structural property of FA_{0.75}Cs_{0.25}PbI₃ under hydrostatic pressure and proposed that there was a direct-indirect bandgap transition in FA_{0.75}Cs_{0.25}PbI₃ under 3 GPa, and the resulting indirect bandgap was 5–7 meV narrower than the direct gap.¹¹⁵ Differently, an indirect-direct bandgap transition was observed in MAPbI₃ single crystal at 325 MPa hydrostatic pressure and the position of the indirect transition was 60 meV below the direct transition. They thought the reduction of Rashba splitting derives from the reduction in local electric field around the Pb atom under pressure.¹¹⁹

b. Defects. In strained perovskites, the enhancement of Pb–I interaction under compressive strain increases the difficulty for I ions to escape from the potential well of Pb atoms, increasing the I

migration barrier, which reduces the density of I vacancies and under-coordinated Pb. Conversely, the weakening of Pb–I interaction deriving from the lengthening of Pb–I bonds and shrinking of I–Pb–I bond angles may increase the density of I vacancies in perovskites. In perovskite band structures, strain pushes up/down VBM, which will change the trap states. Compressive strain causes the ascendance of the VBM, leading the trap states already existing in the sub-gap close to VBM to become shallower-level defects.¹⁰⁶ Therefore, non-radiative recombination of carriers reduces, and carrier lifetimes are improved. Conversely, the trap states shift to a deeper energy level as the VBM shifts downward, increasing non-radiative recombination.

Photoluminescence (PL) spectroscopy is one of the most convenient techniques to characterize the influence of strain to the charge recombination properties of perovskites and thus how strain changes defects in perovskites. In strained perovskites, the PL intensity and carrier lifetime were shown to change significantly.^{65,106,120} Kong *et al.* reported that the compressed MAPbI₃ single crystals exhibited a

TABLE II. Materials of the PV laminate used in the FEM model with the applied material model and thickness.

Layer	Materials	Thickness (mm)	Young's modulus (GPa)	Poisson's ratio (ν)	AQ11
Backsheet	PVF-PET-PVF	0.35	3.5	0.29	
Encapsulant	EVA	0.45	0.11	0.49	
Solar cell	Monocrystalline Si	0.2	130	0.28	
Front cover	Glass	3.2	73	0.23	

⁷⁰⁴ notable red-shift of its absorption edge under \sim 0.3 GPa hydrostatic pressure, and the bandgap narrowing triggered a 70% to \sim 100% ⁷⁰⁵ increase in carrier recombination lifetime.¹⁰⁶ Jones *et al.* combined ⁷⁰⁶ synchrotron scanning XRD measurements and local time-resolved PL ⁷⁰⁷ measurements to study MAPbI₃ films and revealed that local strain ⁷⁰⁸ (tensile strain along in-plane direction) led to an increase in defects ⁷⁰⁹ such as halide vacancies that are associated with local non-radiative ⁷¹⁰ decay. They quantified the trap density with a kinetic model and found ⁷¹¹ that the local strain increased the trap density from 1×10^{16} cm⁻³ to ⁷¹² 7.5×10^{16} cm⁻³.⁶⁵ Notably, their results did not exclude the influence ⁷¹³ of grain boundaries, where defect concentration is higher than that of ⁷¹⁴ grain interior. Furthermore, in perovskite nanoparticles, Zhao *et al.* ⁷¹⁵ observed that much bigger strain results in more strain-induced ⁷¹⁶ defects, leading to lower PL intensity and PL quantum yields (PLQYs) ⁷¹⁷ of nano-scale colloidal CsPbBr₃ perovskite materials.⁸⁷

⁷¹⁸ In addition, in polycrystalline perovskite films, strain was ⁷¹⁹ reported to be responsible for the formation of deep trap states and ⁷²⁰ higher non-radiative recombination rate at grain boundaries. Several ⁷²¹ early calculations based on density functional theory reported that ⁷²² grain boundaries do not introduce deep gap states and are electrically ⁷²³ benign,^{121,122} which is, however, against the experimental observations ⁷²⁴ in the field. PL intensity was generally lower at grain boundaries, and ⁷²⁵ grain boundaries exhibited a faster nonradiative decay.¹²³ Hundreds of ⁷²⁶ passivation molecules have been developed to reduce the deep trap ⁷²⁷ densities.¹²⁴ After passivation, grain boundaries showed high luminescence ⁷²⁸ efficiencies.¹²⁵ Yan *et al.* considered the impact of the change of ⁷²⁹ bond length or lattice constant at the grain boundary areas on the trap ⁷³⁰ states. Their calculation found that the compressive strain with an ⁷³¹ increased I-I coupling strength at grain boundaries pushed the I-I ⁷³² antibonding states into the forbidden gap, making iodide interstitial to ⁷³³ be deep defect states.¹²⁶ Park *et al.* calculated the energy levels of ⁷³⁴ iodine interstitial defects at CsPbBr₃ grain boundaries. They found ⁷³⁵ that when the I-I bond was lengthened at the grain boundaries, the ⁷³⁶ I_i⁺/I_i⁻ levels lowered in energy, making I_i⁺ level deeper states with ⁷³⁷ respect to the conduction band edge and I_i⁻ defects less detrimental ⁷³⁸ than those in the grain interior.¹²⁷

740 IV. SUMMARY AND OUTLOOK

⁷⁴¹ In summary, strain engineering is a powerful and promising ⁷⁴² method to control the properties of perovskites. Under strain, the ⁷⁴³ changes in lead-halide bond lengths and halide-lead-halide bond ⁷⁴⁴ angles will lead to the lattice shrinkage/expansion, or inorganic octahedra ⁷⁴⁵ framework tilting and lattice rotation in the perovskite. Therefore, ⁷⁴⁶ strain engineering can undoubtedly be applied to modulate the band ⁷⁴⁷ structure and carrier dynamics. Meantime, the strain in perovskites ⁷⁴⁸ will decrease the energy difference and increase the energy barrier ⁷⁴⁹ between the perovskite phase and non-perovskite phases, thereby

stabilizing the perovskite phase. Strain changes the perovskite material ⁷⁵⁰ stability due to changes in activation energy of ion migration and trap ⁷⁵¹ state energy level. Especially, compressive strain in perovskites ⁷⁵² increases the activation energy of ion migration, which will hinder the ⁷⁵³ ion migration, thereby inhibiting phase segregation in mixed-halide ⁷⁵⁴ perovskites.⁷⁵⁵

⁷⁵⁶ There are still many open questions to be answered by the perovskite ⁷⁵⁷ community concerning strain. The first question is about strain ⁷⁵⁸ relaxation dynamics. Strain in perovskites would eventually be released ⁷⁵⁹ with the generation of defects such as dislocations or grain boundaries.⁷⁶⁰ The second question to be answered is about the strain distribution on ⁷⁶¹ microscale. Strain may be inhomogeneous across the halide perovskite ⁷⁶² films, and the inhomogeneous distribution of strain on in individual ⁷⁶³ grains or across the films may lead to heterogeneity in carrier transport ⁷⁶⁴ and recombination. Third, there is not enough study yet of how strain ⁷⁶⁵ is introduced in the perovskite materials. Clearly the solvent evaporation ⁷⁶⁶ process and thermal treatment would impact the strain formation, ⁷⁶⁷ and even the solar panel encapsulation process may also introduce ⁷⁶⁸ additional global strain due to the pressure and high temperature to be ⁷⁶⁹ applied. Finally, strain would also be induced in devices in operation ⁷⁷⁰ due to the changes of the environmental conditions. Therefore, the ⁷⁷¹ development of applicable methods to understand the strain-related ⁷⁷² phenomenon is important for the development of efficient and stable ⁷⁷³ perovskite solar modules with high reliability.

774 Experiment and Methods

⁷⁷⁵ The simulation of strain distribution. The simulation was conducted ⁷⁷⁶ by MATLAB. As a first step, we input the geometry of PV ⁷⁷⁷ modules including different layers using geometric primitives, and ⁷⁷⁸ then the geometry is discretized into a collection of finite element ⁷⁷⁹ mesh using tetrahedral elements in 3D. Here, each layer is simulated ⁷⁸⁰ as isotropic material, and the mechanical properties of them are shown ⁷⁸¹ in Table II. Boundary conditions are defined according to the PV ⁷⁸² installation way. In our case, the PV panel was framed at four edges ⁷⁸³ and the mechanical pressure load test with 1000 Pa. At the end, displacement of PV modules was calculated by the partial differential ⁷⁸⁴ equations (PDE). The PDE toolbox provides functions for solving ⁷⁸⁵ structural mechanics, heat transfer mechanical deformations, fluid ⁷⁸⁶ flow, and more.⁷⁸⁷

788 ACKNOWLEDGMENTS

⁷⁸⁹ We thank the National Science Foundation for financial ⁷⁹⁰ support (Grant Nos. DMR-1903981 and ECCS-2050357) and the ⁷⁹¹ Department of the Defense, Defense Threat Reduction Agency ⁷⁹² (Grant No. HDTRA1-20-2-0002).⁷⁹³

794 DATA AVAILABILITY

795 The data that support the findings of this study are available
 796 from the corresponding author upon reasonable request.

797 REFERENCES

798 ¹S. D. Stranks, G. E. Eperon, G. Grancini, C. Menelaou, T. Leijtens, M. J. P.
 799 Alcocer, L. M. Herz, A. Petrozza, and H. J. Snaith, *Science* **342**, 341–344
 800 (2013).

801 ²G. E. Eperon, S. D. Stranks, C. Menelaou, M. B. Johnston, L. M. Herz, and
 802 H. J. Snaith, *Energy Environ. Sci.* **7**(3), 982–988 (2014).

803 ³W.-J. Yin, T. Shi, and Y. Yan, *Appl. Phys. Lett.* **104**(6), 063903 (2014).

804 ⁴D. Shi, V. Adinolfi, R. Comin, M. Yuan, E. Alarousu, A. Buin, Y. Chen, S.
 805 Hoogland, A. Rothenberger, K. Katsiev, Y. Losovyj, X. Zhang, P. A. Dowben,
 806 O. F. Mohammed, E. H. Sargent, and O. M. Bakr, *Science* **347**(6221),
 807 519–522 (2015).

808 ⁵M. M. Lee, J. Teuscher, T. Miyasaka, T. N. Murakami, and H. J. Snaith,
 809 *Science* **338**(6107), 643–647 (2012).

810 ⁶L. Protesescu, S. Yakunin, M. I. Bodnarchuk, F. Krieg, R. Caputo, C. H.
 811 Hendon, R. X. Yang, A. Walsh, and M. V. Kovalenko, *Nano Lett.* **15**(6),
 812 3692–3696 (2015).

813 ⁷M. J. Carnie, C. Charbonneau, M. L. Davies, J. Troughton, T. M. Watson, K.
 814 Wojciechowski, H. Snaith, and D. A. Worsley, *Chem. Commun. (Cambridge)*
 815 **49**(72), 7893–7895 (2013).

816 ⁸J. Burschka, N. Pellet, S. J. Moon, R. Humphry-Baker, P. Gao, M. K.
 817 Nazeeruddin, and M. Grätzel, *Nature* **499**(7458), 316–319 (2013).

818 ⁹D. Liu and T. L. Kelly, *Nat. Photonics* **8**(2), 133–138 (2014).

819 ¹⁰L. Dou, Y. M. Yang, J. You, Z. Hong, W. H. Chang, G. Li, and Y. Yang, *Nat.
 820 Commun.* **5**, 5404 (2014).

821 ¹¹V. Adinolfi, O. Ouellette, M. I. Saidaminov, G. Walters, A. L. Abdelhady, O.
 822 M. Bakr, and E. H. Sargent, *Adv. Mater.* **28**(33), 7264–7268 (2016).

823 ¹²W. Q. Wu, Z. Yang, P. N. Rudd, Y. Shao, X. Dai, H. Wei, J. Zhao, Y. Fang, Q.
 824 Wang, Y. Liu, Y. Deng, X. Xiao, Y. Feng, and J. Huang, *Sci. Adv.* **5**(3),
 825 eaav8925 (2019).

826 ¹³A. Kojima, K. Teshima, Y. Shirai, and T. Miyasaka, *J. Am. Chem. Soc.*
 827 **131**(17), 6050–6051 (2009).

828 ¹⁴NREL. Best Research-Cell Efficiency Chart. (2021). <https://www.nrel.gov/pv/cell-efficiency.html>.

829 ¹⁵C. S. Smith, *Phys. Rev.* **94**(1), 42–49 (1954).

830 ¹⁶J. Welser, J. L. Hoyt, S. Takagi, and J. F. Gibbons, *Proceedings of 1994 IEEE
 831 International Electron Devices Meeting* (■, 1994), pp. 373–376.

832 ¹⁷J. Feng, X. Qian, C.-W. Huang, and J. Li, *Nat. Photonics* **6**(12), 866–872
 833 (2012).

834 ¹⁸G. Tsutsui, S. Mochizuki, N. Loubet, S. W. Bedell, and D. K. Sadana, *AIP Adv.*
 835 **9**(3), 030701 (2019).

836 ¹⁹L. Mao, Q. Meng, A. Ahmad, and Z. Wei, *Adv. Energy Mater.* **7**(23), 1700535
 837 (2017).

838 ²⁰D. Djomani, F. Capitani, J. B. Brubach, E. Calandrini, C. Renard, D. Bouchier,
 839 J. P. Itié, P. Roy, and L. Vincent, *Nanotechnology* **31**(23), 235711 (2020).

840 ²¹L. Vincent, D. Djomani, M. Fakfakh, C. Renard, B. Belier, D. Bouchier, and G.
 841 Patriarche, *Nanotechnology* **29**(12), 125601 (2018).

842 ²²J. Berry, S. Zhou, J. Han, D. J. Srolovitz, and M. P. Haataja, *Nano Lett.* **17**(4),
 843 2473–2481 (2017).

844 ²³S. Song, D. H. Keum, S. Cho, D. Perello, Y. Kim, and Y. H. Lee, *Nano Lett.*
 845 **16**(1), 188–193 (2016).

846 ²⁴Y. M. Niquet, C. Delerue, and C. Krzeminski, *Nano Lett.* **12**(7), 3545–3550
 847 (2012).

848 ²⁵M. Hosseini, M. Elahi, M. Pourfath, and D. Esseni, *IEEE Trans. Electron
 849 Devices* **62**(10), 3192–3198 (2015).

850 ²⁶H. J. Conley, B. Wang, J. I. Ziegler, R. F. Haglund, Jr., S. T. Pantelides, and
 851 K. I. Bolotin, *Nano Lett.* **13**(8), 3626–3630 (2013).

852 ²⁷H. Li, C. Tsai, A. L. Koh, L. Cai, A. W. Contryman, A. H. Fragapane, J. Zhao,
 853 H. S. Han, H. C. Manoharan, F. Abild-Pedersen, J. K. Nørskov, and X. Zheng,
 854 *Nat. Mater.* **15**(3), 364 (2016).

855 ²⁸J. R. Petrie, H. Jeen, S. C. Barron, T. L. Meyer, and H. N. Lee, *J. Am. Chem.
 856 Soc.* **138**(23), 7252–7255 (2016).

857 ²⁹R. U. Chandrasena, W. Yang, Q. Lei, M. U. Delgado-Jaime, K. D. Wijesekara,
 858 M. Golalikhani, B. A. Davidson, E. Arenholz, K. Kobayashi, M. Kobata, F. M.
 859 de Groot, U. Aschauer, N. A. Spaldin, X. Xi, and A. X. Gray, *Nano Lett.* **17**(2),
 860 794–799 (2017).

861 ³⁰Y. Rakita, S. R. Cohen, N. K. Kedem, G. Hodes, and D. Cahen, *MRS
 862 Communications* **5**(4), 623–629 (2015).

863 ³¹A. Ferreira, A. Létoublon, S. Paofai, S. Raymond, C. Ecolivet, B. Rufflé, S.
 864 Cordier, C. Katan, M. I. Saidaminov, and A. Zhumekenov, *Phys. Review Lett.*
 865 **121**(8), 085502 (2018).

866 ³²S. Sun, Y. Fang, G. Kieslich, T. J. White, and A. K. Cheetham, *J. Mater. Chem.
 867 A* **3**(36), 18450–18455 (2015).

868 ³³J. Feng, *APL Mater.* **2**, 081801 (2014).

869 ³⁴J. Zhao, Y. Deng, H. Wei, X. Zheng, Z. Yu, Y. Shao, J. E. Shield, and J. Huang,
 870 *Sci. Adv.* **3**(5616), eaao5616 (2017).

871 ³⁵N. Rolston, K. A. Bush, A. D. Printz, A. Gold-Parker, Y. C. Ding, M. F.
 872 Toney, M. D. McGehee, and R. H. Dauskardt, *Adv. Energy Mater.* **8**(29),
 873 1802139 (2018).

874 ³⁶M. I. Saidaminov, J. Kim, A. Jain, R. Quintero-Bermudez, H. Tan, G. Long, F.
 875 Tan, A. Johnston, Y. Zhao, O. Voznyy, and E. H. Sargent, *Nat. Energy* **3**(8),
 876 648–654 (2018).

877 ³⁷O. Nakatsuka, H. Kitada, Y. Kim, Y. Mizushima, T. Nakamura, T. Ohba, and
 878 S. Zaima, *Japanese J. Appl. Phys.* **50**(5S1), 05ED03 (2011).

879 ³⁸M. Song, K. R. Mundboth, J. A. Szpunar, L. Chen, and R. Feng, *J. Micromech.
 880 Microeng.* **25**(8), 085002 (2015).

881 ³⁹M. J. Hytch and A. M. Minor, *MRS Bull.* **39**(2), 138–146 (2014).

882 ⁴⁰S. Chen and P. Gao, *J. Appl. Phys.* **128**(1), 010901 (2020).

883 ⁴¹Y. Li, W. Zhou, Y. Li, W. Huang, Z. Zhang, G. Chen, H. Wang, G.-H. Wu, N.
 884 Rolston, and R. Vilà, *Joule* **3**(11), 2854–2866 (2019).

885 ⁴²M. U. Rothmann, J. S. Kim, J. Borchert, K. B. Lohmann, C. M. O’Leary, A. A.
 886 Shearer, L. Clark, H. J. Snaith, M. B. Johnston, P. D. Nellist, and L. M. Herz,
 887 *Science* **370**(6516), eabb5940 (2020).

888 ⁴³V. Ozdol, C. Gammer, X. Jin, P. Ercius, C. Ophus, J. Ciston, and A. Minor,
 889 *Appl. Phys. Lett.* **106**(25), 253107 (2015).

890 ⁴⁴J. R. Ferraro and K. Nakamoto, ■ (Academic Press, New York, 1994).

891 ⁴⁵C. Rice, R. J. Young, R. Zan, U. Bangert, D. Wolverson, T. Georgiou, R. Jalil,
 892 and K. S. Novoselov, *Phys. Rev. B* **87**(8), 081307(R) (2013).

893 ⁴⁶M. A. Bissett, M. Tsuji, and H. Ago, *Phys. Chem. Chem. Phys.* **16**(23),
 894 11124–11138 (2014).

895 ⁴⁷C. Fasolato, M. De Luca, D. Djomani, L. Vincent, C. Renard, G. Di Iorio, V.
 896 Paillard, M. Amato, R. Rurali, and I. Zardo, *Nano Lett.* **18**(11), 7075–7084
 897 (2018).

898 ⁴⁸B. Fluegel, A. V. Mialisins, D. A. Beaton, J. L. Reno, and A. Mascarenhas, *Nat.
 899 Commun.* **6**, 7136 (2015).

900 ⁴⁹K. Talit and D. A. Strubbe, *J. Phys. Chem. C* **124**(50), 27287–27299 (2020).

901 ⁵⁰A. Ogura, D. Kosemura, M. Takei, H. Uchida, N. Hattori, M. Yoshimaru, S.
 902 Mayuzumi, and H. Wakabayashi, *Mater. Sci. Eng. B* **159**, 206–211 (2009).

903 ⁵¹M. Ledinský, P. López, B. Niesen, J. Holovský, S.-J. Moon, J.-H. Yum, S. De
 904 Wolf, A. Fejfar, and C. Ballif, *J. Phys. Chem. Lett.* **6**(3), 401–406 (2015).

905 ⁵²M. Ledinský, E. Moulin, G. Bugnon, K. Ganzerová, A. Vetuska, F. Meillaud,
 906 A. Fejfar, and C. Ballif, *Appl. Phys. Lett.* **105**(11), 111106 (2014).

907 ⁵³K. Kitahara, A. Moritani, A. Hara, and M. Okabe, *Jpn. J. Appl. Phys.* **38**(11B),
 908 L1312 (1999).

909 ⁵⁴C. Li, X. Lu, W. Ding, L. Feng, Y. Gao, and Z. Guo, *Acta Crystallogr. Sect. B:
 910 Struct. Sci.* **64**(6), 702–707 (2008).

911 ⁵⁵W. Travis, E. N. K. Glover, H. Bronstein, D. O. Scanlon, and R. G. Palgrave,
 912 *Chem. Sci.* **7**(7), 4548–4556 (2016).

913 ⁵⁶X. Zheng, C. Wu, S. K. Jha, Z. Li, K. Zhu, and S. Priya, *ACS Energy Lett.* **1**(5),
 914 1014–1020 (2016).

915 ⁵⁷C. Wu, K. Chen, D. Guo, S. Wang, and P. Li, *RSC Advances* **8**(6), 2900–2905
 916 (2018).

917 ⁵⁸H. Wang, C. Zhu, L. Liu, S. Ma, P. Liu, J. Wu, C. Shi, Q. Du, Y. Hao, S. Xiang,
 918 H. Chen, P. Chen, Y. Bai, H. Zhou, Y. Li, and Q. Chen, *Adv. Mater.* **31**(48),
 919 e1904408 (2019).

920 ⁵⁹G. Kim, H. Min, K. S. Lee, D. Y. Lee, S. M. Yoon, and S. I. Seok, *Science*
 921 **370**(6512), 108–122 (2020).

922 ⁶⁰E. T. Hoke, D. J. Slotcavage, E. R. Dohner, A. R. Bowring, H. I. Karunadasa,
 923 and M. D. McGehee, *Chem. Sci.* **6**(1), 613–617 (2015).

AQ14

925 ⁶¹J.-S. Park and A. Walsh, *Annu. Rev. Condens. Matter Phys.* **12**, 95–109 (2021).
 926
 927 ⁶²H. Tsai, R. Asadpour, J.-C. Blancon, C. C. Stoumpos, O. Durand, J. W. Strzalka, B. Chen, R. Verduzco, P. M. Ajayan, and S. Tretiak, *Science* **360**(6384), 67–70 (2018).
 928
 929 ⁶³B. Chen, J. Song, X. Dai, Y. Liu, P. N. Rudd, X. Hong, and J. Huang, *Adv. Mater.* **31**(35), e1902413 (2019).
 930
 931 ⁶⁴K. A. Bush, N. Rolston, A. Gold-Parker, S. Manzoor, J. Hausele, Z. J. Yu, J. A. Raiford, R. Cheacharoen, Z. C. Holman, M. F. Toney, R. H. Dauskardt, and M. D. McGehee, *ACS Energy Lett.* **3**(6), 1225–1232 (2018).
 932
 933 ⁶⁵T. W. Jones, A. Osherov, M. Alsari, M. Sponseller, B. C. Duck, Y.-K. Jung, C. Settens, F. Nirouzi, R. Brenes, and C. V. Stan, *Energy Environ. Sci.* **12**(2), 596–606 (2019).
 934
 935 ⁶⁶X. Li, Y. Luo, M. V. Holt, Z. Cai, and D. P. Fenning, *Chem. Mater.* **31**(8), 2778–2785 (2019).
 936
 937 ⁶⁷D. H. Fabini, C. C. Stoumpos, G. Laurita, A. Kaltzoglou, A. G. Kontos, P. Falaras, M. G. Kanatzidis, and R. Seshadri, *Angew. Chem. Int. Ed.* **55**(49), 15392–15396 (2016).
 938
 939 ⁶⁸L. Cojocaru, S. Uchida, Y. Sanehira, V. Gonzalez-Pedro, J. Bisquert, J. Nakazaki, T. Kubo, and H. Segawa, *Chem. Lett.* **44**(11), 1557–1559 (2015).
 940
 941 ⁶⁹T. J. Jacobsson, L. J. Schwan, M. Ottosson, A. Hagfeldt, and T. Edvinsson, *Inorg. Chem.* **54**(22), 10678–10685 (2015).
 942
 943 ⁷⁰C. Ge, M. Hu, P. Wu, Q. Tan, Z. Chen, Y. Wang, J. Shi, and J. Feng, *J. Phys. Chem. C* **122**(28), 15973–15978 (2018).
 944
 945 ⁷¹J. A. Steele, H. Jin, I. Dovgaliuk, R. F. Berger, T. Braeckeveldt, H. Yuan, C. Martin, E. Solano, K. Lejaeghere, and S. M. Rogge, *Science* **365**(6454), 679–684 (2019).
 946
 947 ⁷²D.-J. Xue, Y. Hou, S.-C. Liu, M. Wei, B. Chen, Z. Huang, Z. Li, B. Sun, A. H. Proppe, Y. Dong, M. I. Saidaminov, S. O. Kelley, J.-S. Hu, and E. H. Sargent, *Nat. Commun.* **11**(1), 1514 (2020).
 948
 949 ⁷³Y. Chen, Y. Lei, Y. Li, Y. Yu, J. Cai, M.-H. Chiu, R. Rao, Y. Gu, C. Wang, and W. Choi, *Nature* **577**(7789), 209–215 (2020).
 950
 951 ⁷⁴E. Olsenberg, A. Merdasa, L. Houben, I. Kaplan-Ashiri, A. Rothman, I. G. Scheblykin, E. L. Unger, and E. Joselevich, *Nat. Commun.* **11**(1), 489 (2020).
 952
 953 ⁷⁵E. Shi, B. Yuan, S. B. Shiring, Y. Gao, Akriti, Y. Guo, C. Su, M. Lai, P. Yang, J. Kong, B. M. Savoie, Y. Yu, and L. Dou, *Nature* **580**(7805), 614–620 (2020).
 954
 955 ⁷⁶J.-W. Lee, S. Tan, T.-H. Han, R. Wang, L. Zhang, C. Park, M. Yoon, C. Choi, M. Xu, M. E. Liao, S.-J. Lee, S. Nuryyeva, C. Zhu, K. Huynh, M. S. Goorsky, Y. Huang, X. Pan, and Y. Yang, *Nat. Commun.* **11**(1), 5880 (2020).
 956
 957 ⁷⁷M. Liu, Y. Chen, C.-S. Tan, R. Quintero-Bermudez, A. H. Proppe, R. Munir, H. Tan, O. Voznyy, B. Scheffel, G. Walters, A. P. T. Kam, B. Sun, M.-J. Choi, S. Hoogland, A. Amassian, S. O. Kelley, F. P. García De Arquer, and E. H. Sargent, *Nature* **570**(7759), 96–101 (2019).
 958
 959 ⁷⁸Y. Zhao, J. Duan, Y. Wang, X. Yang, and Q. Tang, *Nano Energy* **67**, 104286 (2020).
 960
 961 ⁷⁹Y. Fu, M. P. Hautzinger, Z. Luo, F. Wang, D. Pan, M. M. Aristov, I. A. Guzei, A. Pan, X. Zhu, and S. Jin, *ACS Central Sci.* **5**(8), 1377–1386 (2019).
 962
 963 ⁸⁰S. Ma, S. H. Kim, B. Jeong, H. C. Kwon, S. C. Yun, G. Jang, H. Yang, C. Park, D. Lee, and J. Moon, *Small* **15**(21), 1900219 (2019).
 964
 965 ⁸¹L. A. Muscarella, E. M. Hutter, F. Wittmann, Y. W. Woo, Y. Jung, L. McGovern, J. Versluis, A. Walsh, H. J. Bakker, and B. Ehrler, *ACS Energy Lett.* **5**(10), 3152–3158 (2020).
 966
 967 ⁸²L. Zhang, L. Wang, K. Wang, and B. Zou, *J. Phys. Chem. C* **122**(27), 15220–15225 (2018).
 968
 969 ⁸³W. Kim, M. S. Jung, S. Lee, Y. J. Choi, J. K. Kim, S. U. Chai, W. Kim, D.-G. Choi, H. Ahn, J. H. Cho, D. Choi, H. Shin, D. Kim, and J. H. Park, *Adv. Energy Mater.* **8**(10), 1702369 (2018).
 970
 971 ⁸⁴G. Liu, L. Kong, W. Yang, and H.-k. Mao, *Mater. Today* **27**, 91–106 (2019).
 972
 973 ⁸⁵Q. Tu, I. Spanopoulos, S. Hao, C. Wolverton, M. G. Kanatzidis, G. S. Shekhatwati, and V. P. Dravid, *ACS Energy Lett.* **4**(3), 796–802 (2019).
 974
 975 ⁸⁶Q. Zhao, A. Hazarika, L. T. Schelhas, J. Liu, E. A. Gaulding, G. Li, M. Zhang, M. F. Toney, P. C. Sercel, and J. M. Luther, *ACS Energy Lett.* **5**(1), 238–247 (2020).
 976
 977 ⁸⁷J. Zhao, M. Liu, L. Fang, S. Jiang, J. Zhou, H. Ding, H. Huang, W. Wen, Z. Luo, Q. Zhang, X. Wang, and C. Gao, *J. Phys. Chem. Lett.* **8**(13), 3115–3121 (2017).
 978
 979 ⁸⁸V. Wadhawan, *Bull. Mater. Sci.* **6**(4), 733–753 (1984).
 980
 981 ⁸⁹E. K. Salje, *Annu. Rev. Mater. Res.* **42**, 265–283 (2012).
 982
 983 ⁹⁰T.-C. Wei, H.-P. Wang, T.-Y. Li, C.-H. Lin, Y.-H. Hsieh, Y.-H. Chu, and J.-H. He, *Adv. Mater.* **29**(35), 1701789 (2017).
 984
 985 ⁹¹Y. Zhou, L. You, S. Wang, Z. Ku, H. Fan, D. Schmidt, A. Rusydi, L. Chang, L. Wang, P. Ren, L. Chen, G. Yuan, L. Chen, and J. Wang, *Nat. Communications* **7**(1), 11193 (2016).
 986
 987 ⁹²N. Rolston, R. Bennett-Kennett, L. T. Schelhas, J. M. Luther, J. A. Christians, J. J. Berry, and R. H. Dauskardt, *Science* **368**(6488), eaay8691 (2020).
 988
 989 ⁹³S. A. Kalogirou, *Solar Energy Engineering: Processes and Systems*. (Academic Press, 2013).
 990
 991 ⁹⁴NASA Earth Observatory, <https://earthobservatory.nasa.gov/biome/biodesert.php>.
 992 ⁹⁵UC Museum of Paleontology, <https://ucmp.berkeley.edu/exhibits/biomes/deserts.php>.
 993 ⁹⁶T. Markvart and A. McEvoy, *Practical Handbook of Photovoltaics: Fundamentals and Applications* (Elsevier, 2003).
 994 ⁹⁷A. Alateeq, Buckling effect on the performance of solar cells under different loading conditions (2018). <https://lib.dr.iastate.edu/creativecomponents/23/>.
 995
 996 ⁹⁸U. Eitner, Thermomechanics of photovoltaic modules (2011). <https://openda-ta.uni-halle.de/handle/1981185920/7357>.
 997
 998 ⁹⁹M. T. Zarmai, N. N. Ekere, C. F. Oduoza, and E. H. Amalu, *Rob. Comput.-Integrated Manuf.* **47**, 37–43 (2017).
 999 ¹⁰⁰S. Liu, S. Sun, C. K. Gan, A. G. d. Águila, Y. Fang, J. Xing, T. T. H. Do, T. J. White, H. Li, W. Huang, and Q. Xiong, *Sci. Adv.* **5**(9445), eaav9445 (2019).
 1000
 1001 ¹⁰¹B. Murali, E. Yengel, W. Peng, Z. Chen, M. S. Alias, E. Alarousu, B. S. Ooi, V. Burlakov, A. Goriely, and M. Eddaoudi, *J. Phys. Chem. Lett.* **8**(1), 137–143 (2017).
 1002
 1003 ¹⁰²X. Lu, W. Yang, Q. Jia, and H. Xu, *Chem. Sci.* **8**(10), 6764–6776 (2017).
 1004 ¹⁰³L. Wang, K. Wang, and B. Zou, *J. Phys. Chem. Lett.* **7**(13), 2556–2562 (2016).
 1005
 1006 ¹⁰⁴T. Chen, B. J. Foley, C. Park, C. M. Brown, L. W. Harriger, J. Lee, J. Ruff, M. Yoon, J. J. Choi, and S.-H. Lee, *Sci. Adv.* **2**(10), e1601650 (2016).
 1007
 1008 ¹⁰⁵L. Guo, G. Xu, G. Tang, D. Fang, and J. Hong, arXiv preprint [arXiv:2001.01041](https://arxiv.org/abs/2001.01041) (2020).
 1009 ¹⁰⁶L. Kong, G. Liu, J. Gong, Q. Hu, R. D. Schaller, P. Dera, D. Zhang, Z. Liu, W. Yang, and K. Zhu, *Proc. Nat. Acad. Sci. U.S.A.* **113**(32), 8910–8915 (2016).
 1010
 1011 ¹⁰⁷D. J. Dunstan, *J. Mater. Sci.: Mater. Electron.* **8**, 337–375 (1997).
 1012
 1013 ¹⁰⁸S. R. Lee, D. D. Koleske, K. C. Cross, J. A. Floro, K. E. Waldrup, A. T. Wise, and S. Mahajan, *Appl. Phys. Lett.* **85**(25), 6164–6166 (2004).
 1014
 1015 ¹⁰⁹L.-y Huang and W. R. Lambrecht, *Phys. Rev. B* **88**(16), 165203 (2013).
 1016
 1017 ¹¹⁰R. Prasanna, A. Gold-Parker, T. Leijtens, B. Conings, A. Babayigit, H.-G. Boyen, M. F. Toney, and M. D. McGehee, *J. Am. Chem. Soc.* **139**(32), 11117–11124 (2017).
 1018
 1019 ¹¹¹C. Grote and R. F. Berger, *J. Phys. Chem. C* **119**(40), 22832–22837 (2015).
 1020
 1021 ¹¹²G. Liu, L. Kong, J. Gong, W. Yang, H. k Mao, Q. Hu, Z. Liu, R. D. Schaller, D. Zhang, and T. Xu, *Adv. Funct. Mater.* **27**(3), 1604208 (2017).
 1022
 1023 ¹¹³Y. Jiao, F. Ma, H. Wang, J. Bell, and A. Du, *Part. Part. Syst. Charact.* **34**(4), 1600288 (2017).
 1024
 1025 ¹¹⁴C. Zhu, X. Niu, Y. Fu, N. Li, C. Hu, Y. Chen, X. He, G. Na, P. Liu, H. Zai, Y. Ge, Y. Lu, X. Ke, Y. Bai, S. Yang, P. Chen, Y. Li, M. Sui, L. Zhang, H. Zhou, and Q. Chen, *Nat. Commun.* **10**(1), 815 (2019).
 1026
 1027 ¹¹⁵D. Ghosh, A. Aziz, J. A. Dawson, A. B. Walker, and M. S. Islam, *Chem. Mater.* **31**(11), 4063–4071 (2019).
 1028
 1029 ¹¹⁶J. Yin, P. Maity, L. Xu, A. M. El-Zohry, H. Li, O. M. Bakr, J.-L. Brédas, and O. F. Mohammed, *Chem. Mater.* **30**(23), 8538–8545 (2018).
 1030
 1031 ¹¹⁷E. M. Hutter, M. C. Gélvez-Rueda, A. Osherov, V. Bulović, F. C. Grozema, S. D. Stranks, and T. J. Savenije, *Nat. Mater.* **16**(1), 115–120 (2017).
 1032
 1033 ¹¹⁸F. Zheng, L. Z. Tan, S. Liu, and A. M. Rappe, *Nano Lett.* **15**(12), 7794–7800 (2015).
 1034
 1035 ¹¹⁹T. Wang, B. Daiber, J. M. Frost, S. A. Mann, E. C. Garnett, A. Walsh, and B. Ehrler, *Energy Environ. Sci.* **10**(2), 509–515 (2017).
 1036
 1037 ¹²⁰K. M. Boopathi, B. Martín-García, A. Ray, J. M. Pina, S. Marras, M. I. Saidaminov, F. Bonaccorso, F. Di Stasio, E. H. Sargent, L. Manna, and A. L. Abdellahy, *ACS Energy Lett.* **5**(2), 642–649 (2020).
 1038
 1039 ¹²¹W.-J. Yin, T. Shi, and Y. Yan, *Adv. Mater.* **26**(27), 4653–4658 (2014).
 1040
 1041 ¹²²W.-J. Yin, J.-H. Yang, J. Kang, Y. Yan, and S.-H. Wei, *J. Mater. Chem. A* **3**(17), 8926–8942 (2015).
 1042
 1043 ¹²³E. K. Salje, *Annu. Rev. Mater. Res.* **42**, 265–283 (2012).
 1044
 1045 ¹²⁴T.-C. Wei, H.-P. Wang, T.-Y. Li, C.-H. Lin, Y.-H. Hsieh, Y.-H. Chu, and J.-H. He, *Adv. Mater.* **29**(35), 1701789 (2017).
 1046
 1047 ¹²⁵Y. Zhou, L. You, S. Wang, Z. Ku, H. Fan, D. Schmidt, A. Rusydi, L. Chang, L. Wang, P. Ren, L. Chen, G. Yuan, L. Chen, and J. Wang, *Nat. Communications* **7**(1), 11193 (2016).
 1048
 1049 ¹²⁶N. Rolston, R. Bennett-Kennett, L. T. Schelhas, J. M. Luther, J. A. Christians, J. J. Berry, and R. H. Dauskardt, *Science* **368**(6488), eaay8691 (2020).
 1050
 1051 ¹²⁷M. T. Zarmai, N. N. Ekere, C. F. Oduoza, and E. H. Amalu, *Rob. Comput.-Integrated Manuf.* **47**, 37–43 (2017).
 1052
 1053 ¹²⁸X. Lu, W. Yang, Q. Jia, and H. Xu, *Chem. Sci.* **8**(10), 6764–6776 (2017).
 1054
 1055 ¹²⁹L. Kong, G. Liu, J. Gong, Q. Hu, R. D. Schaller, P. Dera, D. Zhang, Z. Liu, W. Yang, and K. Zhu, *Proc. Nat. Acad. Sci. U.S.A.* **113**(32), 8910–8915 (2016).
 1056
 1057 ¹³⁰D. Ghosh, A. Aziz, J. A. Dawson, A. B. Walker, and M. S. Islam, *Chem. Mater.* **31**(11), 4063–4071 (2019).
 1058

1059 ¹²³D. W. De Quilettes, S. M. Vorpahl, S. D. Stranks, H. Nagaoka, G. E. Eperon, M. E.
1060 Ziffer, H. J. Snaith, and D. S. Ginger, *Science* **348**(6235), 683–686 (2015).
1061 ¹²⁴B. Chen, P. N. Rudd, S. Yang, Y. Yuan, and J. Huang, *Chem. Soc. Rev.* **48**(14),
1062 3842–3867 (2019).
1063 ¹²⁵M. Abdi-Jalebi, Z. Andaji-Garmaroudi, S. Cacovich, C. Stavrakas, B. Philippe,
1064 J. M. Richter, M. Alsari, E. P. Booker, E. M. Hutter, A. J. Pearson, S. Lilliu, T. J.
Savenije, H. Rensmo, G. Divitini, C. Ducati, R. H. Friend, and S. D. Stranks, **1065**
Nature **555**(7697), 497–501 (2018).
¹²⁶Y. Yan, W.-J. Yin, T. Shi, W. Meng, and C. Feng, *Organic-Inorganic Halide* **1067**
Perovskite Photovoltaics (Springer, 2016), pp. 79–105.
¹²⁷J.-S. Park, J. Calbo, Y.-K. Jung, L. D. Whalley, and A. Walsh, *ACS Energy Lett.* **1069**
4(6), 1321–1327 (2019).

Author Proof